EES Catalysis

REVIEW ARTICLE

View Article Online
View Journal | View Issue

Cite this: *EES Catal.*, 2024, 2, 448

Metal halide perovskites for CO_2 photoreduction: recent advances and future perspectives

Zhongliang Dong, Bowen Li, Yinlong Zhu* and Wanlin Guo

CO_2 emission has inarguably become one of the greatest challenges ever faced by mankind since industrial revolution. Techniques aiming at capture, storage and utilization of CO_2 have attracted tremendous interest from both industry and academia. Thermal, electrical and photo-catalytic conversion of CO_2 to value-added chemicals and fuels is the most well-known approach for CO_2 utilization. In particular, photocatalytic reduction of CO_2 (CO_2PR) directly employs solar energy as the driving force to activate CO_2, yielding various products including CO, CH_4 and C_{2+} hydrocarbons. CO_2PR, which mimics photosynthesis occurring in nature, is also regarded as "artificial photosynthesis" and is believed to be a promising approach toward carbon neutral economy. Recently, metal halide perovskites (MHPs) have emerged as potential photocatalysts for CO_2PR, owing to their flexible structures and excellent photoelectronic properties. This review presents a comprehensive overview of state-of-the-art developments in MHP-based catalysts for CO_2PR. Firstly, the crystal structures and photoelectric properties of MHPs are reviewed in detail, as they are the key factors determining CO_2PR catalytic performance. Secondly, design strategies to promote the catalytic efficiency of CO_2PR to CO conversion for both lead-based and lead-free MHPs are discussed, including morphological modifications, co-catalyst modifications, ion doping and crystal plane modifications. Thirdly, this review addresses MHP-based CO_2PR to CH_4 and C_{2+} products, with special emphasis on approaches adopted to promote specific product selectivity. Lastly, our perspectives and opinions are given on current research challenges and future directions for CO_2PR, which we consider are critical for its industrialization.

Received 3rd August 2023,
Accepted 4th January 2024

DOI: 10.1039/d3ey00187c

rsc.li/eescatalysis

Broader context

Photocatalytic reduction of CO_2 into value-added chemicals (*i.e.*, artificial photosynthesis) is regarded as a fascinating approach to simultaneously solving global warming and energy crisis. As a class of newly emerged semiconductors, metal halide perovskites (MHPs) have attracted great interest in the field of CO_2 photoreduction in recent years due to their flexible structures and excellent photoelectronic properties. In this review, we present a comprehensive overview of recent advances in MHP-based catalysts for CO_2 photoreduction (CO_2PR). We start with a description of the crystal structure and photoelectric properties of MHPs, which are key to CO_2PR catalytic performance. Then, strategies (*e.g.*, morphological modifications, co-catalyst modifications, ion doping, crystal plane modifications, *etc.*) for lead-based and lead-free MHP materials to improve the efficiency of CO_2PR to CO conversion are systematically summarized. In particular, a detailed discussion on MHP-based CO_2PR to CH_4 and C_{2+} products (with higher economic value) is further presented, with special emphasis on the designed methods for promoting selectivity. Finally, some concluding remarks and an outlook on future challenges and prospects are provided to point out the possible research directions in MHP-based photocatalysts for CO_2PR.

1. Introduction

Over-reliance on the depleting fossil fuels as the main energy source is one of the major problems hindering the transformation toward sustainable economy, while leading to extensive CO_2 emission and causing climate changes at the same time. In response to this daunting challenge, new techniques and process protocols have been developed in various industries to reduce energy consumption, and governments across the globe are promoting the usage of renewable energy sources as clean and green alternatives to conventional fossil fuels. Artificial photosynthesis technology, which utilizes the inexhaustible, green, and pollution-free sunlight to initiate chemical reactions, shows great potential in reducing atmospheric CO_2

Institute for Frontier Science, Key Laboratory for Intelligent Nano Materials and Devices of the Ministry of Education, Nanjing University of Aeronautics and Astronautics, Nanjing 210016, China. E-mail: zhuyl1989@nuaa.edu.cn

emission by converting it into valuable solar fuels.[1,2] Since CO_2 is a thermodynamically stable molecule (the dissociation energy of C═O is about 750 kJ mol^{-1}),[3] the major challenge in CO_2 photocatalysis is to find a photocatalyst that can effectively activate and reduce CO_2. In 1979, Inoue *et al.* reported that various semiconductors could act as photocatalysts to reduce CO_2 in aqueous solution.[4] Since then, many nanostructured materials (*e.g.*, metal oxides,[5,6] metal sulfides[7] and metal halide perovskites (MHPs)) have been developed for photocatalytic CO_2 reduction reaction (referred to as CO_2PR in the following discussions).[8,9] Among them, extensive research works are focusing on TiO_2 and its derivatives, owing to their unique properties including non-toxicity, ease of manufacture, and outstanding photochemical stability.[10] Despite these advantages, the application of TiO_2 catalysts is limited by their inherent large bandgap, which restricts the ability to harvest solar energy over a wide spectrum. In fact, CO_2PR by TiO_2 can only occur in the ultraviolet (UV) range,[11] greatly limiting the efficiency in utilizing solar energy. Recently, organic–inorganic halide perovskites have drawn great attention in the field of photoelectricity, serving as the key component for solar cells, light-emitting diodes (LEDs), photodetectors, X-rays and lasers.[12–22] For example, major breakthroughs have been achieved with perovskite solar cells, with the power conversion efficiency increasing from 3.8% in 2009 to 25.7% in 2023.[23] Superior photoelectric properties and favorable carrier mobility are responsible for the impressive performance of perovskite solar cells.[24] Moreover, the efficiency of green and red perovskite LEDs also reaches over 20% and 1.1%, respectively.[25,26] At the same time, the performance of MHP-based lasers, photodetectors and X-ray detectors is also developing at a rapid pace. Despite numerous advances achieved, the organic groups of most organic–inorganic perovskite materials are extremely sensitive to the environment, limiting their application under industrial conditions.

In recent years, MHPs have gradually emerged as intriguing all-inorganic perovskite materials for photoelectronic and energy conversion applications. With metal cations replacing organic cations, MHPs have a greater extinction coefficient than conventional semiconductor nanocrystals and can withstand more defects. Furthermore, the rich structural diversity allows accurate tuning of the bandgap, thus improving the light capture ability. Based on reaction thermodynamics, efficient photocatalysis requires a good match between the electronic energy band (EB) structure of the catalyst and the redox potential of the reaction. In Fig. 1, the relative positions of the conduction band (CB) and valence band (VB) for the majority of halide perovskites are depicted. It is clearly illustrated that the relative positions of the CB of MHPs are sufficiently negative for H_2 generation, CO_2 reduction, aerobic oxidation and organic matter degradation (*via* superoxide radicals). On the basis of this plot, halide perovskites are seen as a promising candidate for CO_2PR. The CB for most MHPs is more negative than the CO_2 reduction potential, which is a prerequisite and essential condition for CO_2 reduction to occur.[27] Fig. 2 demonstrates the four key steps for CO_2PR, namely light capture, generation and separation of photogenerated carriers, CO_2 adsorption and product desorption.[28] By optimizing these key steps, the overall photocatalytic activity for CO_2 reduction can be improved. For example, higher molar extinction coefficients of MHPs allow them to capture light more effectively, hence leading to better catalytic performances. The molar extinction coefficient of $CsPbX_3$ (X denotes a halide ion) is nearly 10 times higher than that of CdSe nanocrystals with a similar bandgap. Under the same light conditions, the high molar extinction coefficient means that $CsPbX_3$ nanocrystals can capture more sunlight for photocatalysis. Moreover, MHPs generally have a low exciton binding energy (E_b), implying that excitons are more likely to dissociate into free electrons and holes, further facilitating photocatalytic reactions.[29] Nonetheless, strong recombination of photogenerated charge carriers limits the catalytic performance of pristine MHPs, and effective photoreduction of the chemically inert CO_2 with high catalytic activity and product selectivity is still difficult to achieve. Development of efficient photocatalysts remains a key challenge and has attracted research interest across the globe. Novel design strategies are in need, together with more detailed understanding of the reaction mechanism, to develop highly active, selective, and stable photocatalytic systems based on MHPs.

To date, there have been several excellent reviews providing in-depth summaries on MHPs in photocatalysis, discussing the overall photocatalytic performance, stability, and lead toxicity issues.[29–37] However, these reviews mainly focus on hydrogen

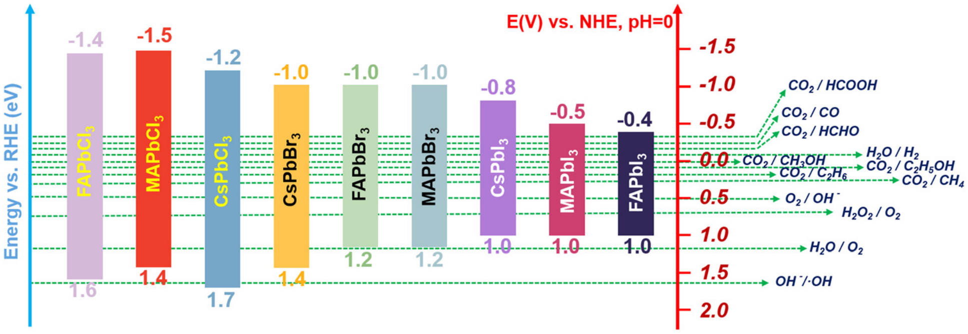

Fig. 1 Band edge positions of halide perovskites relative to reversible hydrogen electrode (RHE).

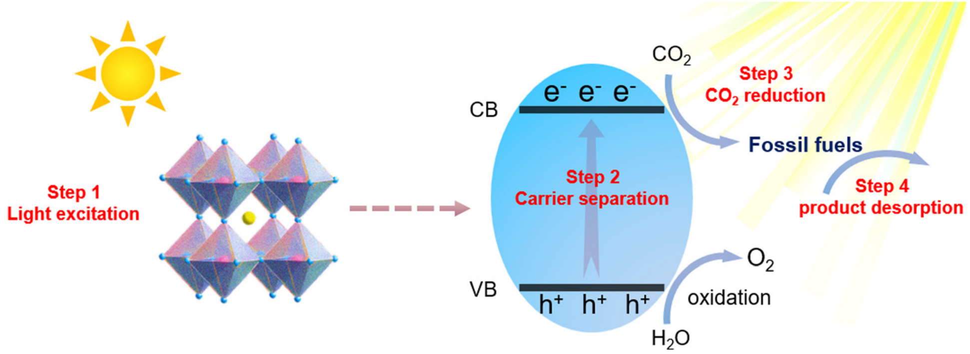

Fig. 2 Schematic diagram of photoreduction of MHPs.

production reaction, pollutant degradation, and other applications. Strategies for the advanced photocatalytic reduction of CO_2 to CO are studied to a lesser extent. Moreover, reviews exploring CO_2PR toward CH_4 and C_{2+} products with higher added values are rarely summarized. In view of recent advances, we believe it is necessary to give a comprehensive overview of the state-of-the-art materials and design strategies in MHP catalyzed CO_2PR. In this review, we first describe the crystal structure and photoelectric properties of MHPs. Following that, detailed discussions are made on the relevant advances accomplished with lead-based and lead-free MHP materials, focusing on strategies to improve the CO_2 photoconversion efficiency to CO. More importantly, the CO_2 photoreduction to CH_4 and C_{2+} products (which are more economically valuable) based on MHP-catalysts is also discussed. Lastly, our insights into future research directions are provided, addressing the urgent challenges that need to be pursued in order to maximize the potential of MHPs in promoting sustainable development and facilitating their practical applications.

2. Structures and properties of MHPs

2.1 Crystal structures of MHPs

The structure of a material serves as a crucial determinant of its physical and chemical properties, and any variation in its structural arrangement can make a profound impact on its performance. Therefore, a comprehensive understanding of the crystal structure of MHPs is essential to accurately predict and fine-tune their optical, electronic, and catalytic properties. It is generally accepted that the chemical formula of perovskites is ABX_3, in which the A-site cation is 12-fold coordinated and the B-site cation is 6-fold coordinated. Typically, perovskite structures are cubic (Fig. 3a) or octahedral in shape (Fig. 3b).[38] X represents the halide elements Cl, Br, and I, and B refers to metal ions like Pb^{2+}, Ge^{2+}, Sn^{2+}, and Bi^{2+}. In these ions, the A and B site ions can be partially replaced by ions with similar radius, while the crystal structure remains essentially unchanged. Depending on whether the A-site ions contain organic groups, they can be divided into two categories: organic–inorganic hybrid perovskites (organic ions in the A-site, such as $CH_3NH_3^+$, methylammonium ion (MA^+), formamidine ion (FA^+)) and all-inorganic perovskites (only inorganic ions in the A-site, such as Cs^+, K^+, Rb^+). It is worth noting that the majority of research efforts in the realm of MHPs have been devoted to exploring the fascinating properties of lead halide perovskites (LHPs) featuring an $APbX_3$ structure,[39,40] due to the exceptional photoelectric properties. Additionally, the remarkable potential of LHPs for various applications such as solar cells, LEDs and photodetectors has made them a focal point of research efforts.[41–47] According to the concept of the Goldschmidt tolerance factor, which involves close packing of ions, only MA^+, FA^+ and Cs^+ can stabilize the 3D PbX_6 framework, because they are geometrically adapted in the A-site of the twelve-coordinates.[40] However, evidence from previous studies

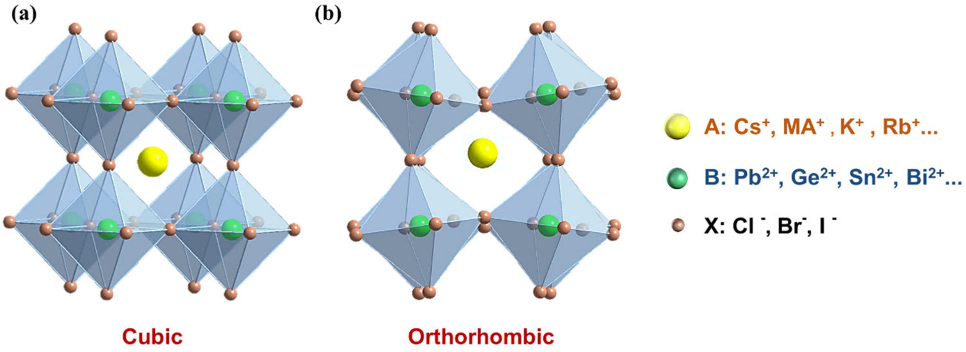

Fig. 3 (a) Cubic and (b) orthorhombic crystal structures of 3D ABX_3 perovskites.

has shown that the crystal structure of $APbX_3$ can be irreversibly damaged and decomposed in the presence of moisture, photothermal radiation and polar solvents, which limits their application in many fields.[48–51] Therefore, exploring more structurally stable $APbX_3$ or surface modified stable materials is an important research trend in the future.

2.2 Photoelectric properties of MHPs

The excellent photoelectric properties of MHPs are primarily attributed to their unique structural characteristics. As described above, their highly ordered and symmetrical lattice three-dimensional network provides a favorable environment for efficient charge transport and light absorption, which makes them ideal for photocatalytic applications. These properties include favorable bandgaps for extended absorption of visible light, high charge carrier mobility, and long charge diffusion length that results in a reduced recombination rate of electron–hole pairs. Recent reports[52–61] have highlighted these properties, which are important factors supporting the potentially superior photocatalytic performance of MHPs. Specifically, MHPs exhibit (1) a high optical absorption coefficient with easily tunable bandgaps, (2) a long carrier diffusion length and suppressed recombination rate, which improve carrier lifetime, and (3) a well-balanced charge transfer suitable for redox reactions.

2.2.1 Flexible and adjustable bandgap. The enhanced light absorption of MHPs compared to conventional semiconductors (*e.g.*, TiO_2) has been found to contribute to the improved photocarrier conversion efficiency, as demonstrated in many perovskite-based solar cells.[60] In order to maximize the optical absorption of a photocatalytic material, it is necessary to possess an appropriate bandgap. Theoretically, by reducing the bandgap value, the absorption spectrum of the visible light becomes wider and the efficiency of light utilization can be increased.[61] The energy level of MHPs is related to their bandgap, which is composed of the conduction band minimum (CBM) and the valence band maximum (VBM). For MHPs, the VBM consists of an antibonding hybrid state between the 6s orbitals of the B divalent cation and the *n*p orbitals of X (n = 3, 4 and 5 for Cl, Br and I, respectively), with the latter playing a dominant role. The CBM is an antibonding hybrid state of the 6p orbitals of B and the *n*p orbitals of X, and the main contributor is from the 6p orbitals of B.[62,63] As A-site ions have little impact on the VBM or CBM, the bandgap of MHPs is frequently adjusted by mixing or modifying B and X-site ions. Adjustable bandgap provides the opportunity to regulate the energy band edge and achieve highly efficient photocatalysis in various applications. Additionally, the absorption spectrum of MHPs can be tuned from visible light to near-infrared (NIR) irradiation utilizing the quantum confinement effect. For example, Protesescu *et al.* first reported that the optical absorption and emission spectra of colloidal $CsPbX_3$ NCs (Fig. 4a and b) can be tuned by adjusting their composition (proportion of halides in mixed NCs) and particle size (quantum-size effect) to respond across the visible spectral region.[64] Guo *et al.* demonstrated that $CsPb(Br_x/Cl_{1-x})_3$ exhibits a wide absorption range for visible light from 400 to 700 nm, with a gradual shift of the absorption peak from 520 nm ($CsPbBr_3$) to 420 nm ($CsPbCl_3$) by adjusting the value of X (Fig. 4c).[65] At the same time, Fig. 4d shows an increase in E_g values from 2.33 to 2.98 eV for $CsPb(Br_x/Cl_{1-x})_3$ (x = 1, 0.7, 0.5, 0.3, 0) with a direct bandgap.[65] All of the above evidence suggests that the use of hybrid halides is a viable strategy for modulating the absorption diversity and bandgap in perovskite spectroscopy.

2.2.2 Long carrier lifetime. Under thermal equilibrium conditions, electrons are continuously excited from the valence band to the conduction band to produce electron–hole pairs. At the same time, electron–hole pairs keep disappearing because the recombination of carriers makes the carriers disappear gradually, and the average existence time of such carriers is called carrier lifetime.[64] At equilibrium, the production rate of electrons and holes is equal to the recombination rate, so that the density of carriers in the semiconductor remains constant. Thus, a higher equilibrium carrier concentration favours an increase in carrier lifetime and diffusion length. In the process of photocatalytic reaction, the separation and transport of electrons are the main considerations for the improved catalytic performance. Longer carrier lifetime implies high charge mobility, which is a key advantage for semiconductors. MHPs have been reported to have stable equilibrium carrier concentrations and long carrier lifetime beyond those of commonly used photoelectric materials,[65] as well as beneficial interfacial charge transfer kinetics and still undiscovered electron injection kinetics advantages.[67]

2.2.3 High equilibrium carrier concentration. Generally, the equilibrium carrier concentration refers to the number of electrons and holes in a material that are present in thermodynamic equilibrium at a given temperature. At equilibrium, the rate of generation of free charge carriers (electrons and holes) through excitation processes is balanced by the rate of recombination of those carriers, resulting in a constant density of free carriers in the material. The equilibrium carrier concentration is a critical parameter in determining the electrical and optical properties of a semiconductor material. It is influenced by factors such as the doping level of the material, its intrinsic carrier concentration, the temperature, and the energy gap between the valence and conduction bands.[68] One of the advantages of MHPs is their high equilibrium carrier concentration, which is several orders of magnitude higher than that of conventional semiconductors such as silicon. High carrier concentration originates from the unique crystal structure of MHPs, which consists of alternating layers of metal halide octahedra and organic cations.[69] The high carrier concentration in MHPs is beneficial for many photoelectric applications. For example, in solar cells, the high carrier concentration leads to a high open-circuit voltage and short-circuit current, resulting in high power conversion efficiency. In LEDs, the high carrier concentration enables efficient radiative recombination of electrons and holes, leading to bright and efficient emission. Moreover, the high carrier concentration in MHPs also leads to long carrier diffusion lengths, which enable efficient extraction and collection of charge carriers, reducing the recombination

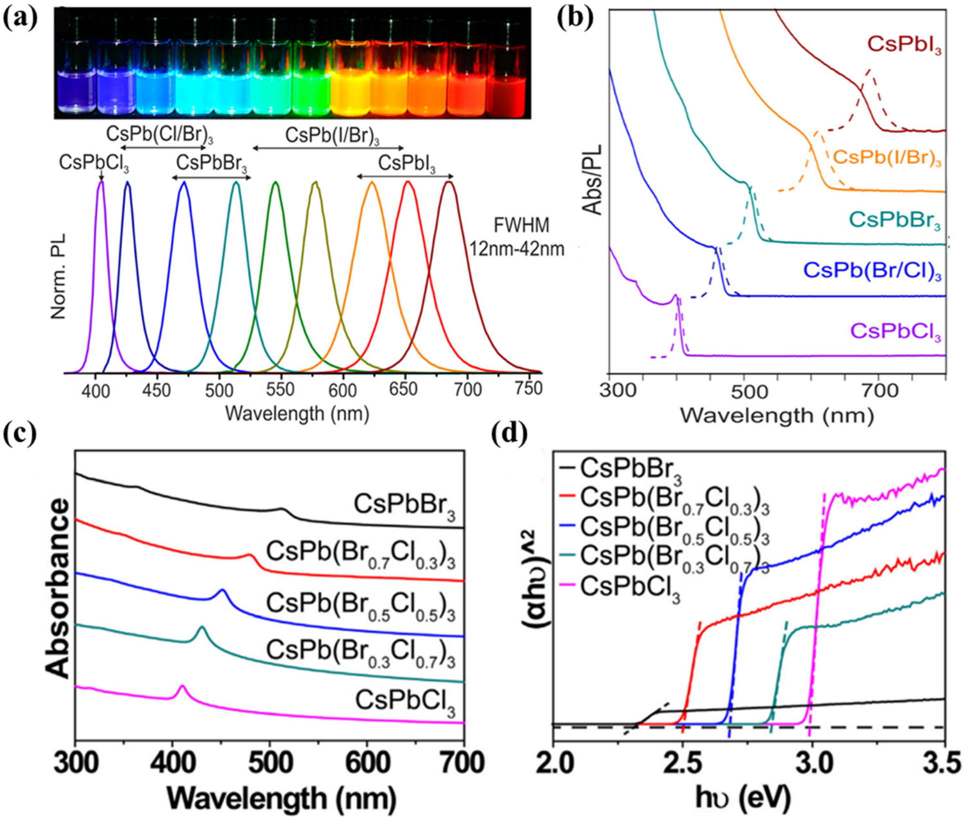

Fig. 4 (a) Colloidal halide perovskite CsPbX$_3$ NCs (X = Cl, Br, and I) exhibit size- and composition-tunable bandgap energies covering the entire visible spectral region with narrow and bright emission.[64] (b) Typical optical absorption and PL spectra of CsPbX$_3$ NCs.[64] (c) UV-vis absorption spectra and (d) $(\alpha h\upsilon)^2$ *versus* $h\upsilon$ curves of CsPb(Br$_x$/Cl$_{1-x}$)$_3$ (x = 1, 0.7, 0.5, 0.3, 0) materials.[65]

losses. Overall, the high equilibrium carrier concentration in MHPs is a significant advantage that makes them promising candidates for various photoelectric applications, offering exceptional performance and potential for future technological advancements.

3. MHP materials for the photoreduction of CO_2 to CO as the main product

To date, several technologies have been developed to convert CO_2 into hydrocarbons or high value-added chemicals, such as thermocatalysis, biocatalysis, electrocatalysis, and photocatalysis. Different from the conventional thermocatalytic CO_2 reduction requiring high temperature and pressure conditions, the photocatalytic CO_2 reduction process simulates natural photosynthesis using sunlight and a photocatalyst to catalyze the conversion of CO_2 and water, which is also named the artificial photosynthesis. Compared to conventional thermocatalytic CO_2 reduction, photocatalytic CO_2 reduction has the following advantages: (1) photocatalytic CO_2 reduction reaction relies solely on solar energy as the external energy input; (2) the reaction utilizes water and CO_2 as raw materials which are abundant and easily accessible; (3) the reaction is free of secondary pollution; and (4) photocatalytic CO_2 reduction enables the synthesis of solar fuels and high value-added chemicals at ambient temperature and pressure. Thus, photocatalytic CO_2 reduction is often regarded as one of the most promising solutions to solve the energy crisis and environmental problems. Since photocatalytic CO_2 reduction is a multielectron transfer process involving various reaction pathways, it is challenging to produce specific products with high selectivity. Photocatalysis (using single atoms, metal oxides, sulfides, nitrides, *etc.*) can be performed in a purely gas phase system or solution system, generating the main products including both C_1 (*e.g.*, CO, CH_4, HCOOH, CH_3OH) and C_{2+} (*e.g.*, C_2H_4, C_2H_6, C_2H_5OH, C_3H_6) chemicals. The reaction conditions and the corresponding products are displayed in Table 1. When employing MHPs as catalysts, CO_2 tends to be reduced to CO and CH_4, accompanied by the side reaction of H_2 evolution. In a typical CO_2PR system, the total electron consumption rate and the electron consumption rate for the reduction of CO_2 to carbon products are considered as $R_{\text{total electron}} = 2R(\text{CO}) + 8R(\text{CH}_4) + 2R(\text{H}_2)$ and $R\text{CO}_{2\,\text{reduction}} = 2R(\text{CO}) + 8R(\text{CH}_4)$, respectively. Thus, the selectivity of CO_2 reduction can be calculated as $(R\text{CO}_{2\,\text{reduction}})/(R_{\text{total electron}}) \times 100\%$. To evaluate the performance of photocatalysts, electron consumption rate and product selectivity are two important parameters.

As mentioned above, MHPs are extensively applied in photoelectric devices due to their flexible and adjustable bandgap, long carrier lifetime, and high equilibrium carrier

Table 1 The theoretical equilibrium potential (E^0, V *vs.* NHE at pH = 7) and redox equation for the conversion of CO_2 to different products

Reaction equation	Reduction products	E^0 (V)
$CO_2 + e^- = CO_2^-$	Carbonate anion radical	−1.90
$CO_2 + 2H^+ + 2e^- = CO(g) + H_2O$	Carbon monoxide	−0.53
$2CO_2 + 14H^+ + 2e^- = C_2H_6(g) + 4H_2O$	Ethane	−0.27
$CO_2 + 8H^+ + 8e^- = CH_4(g) + 2H_2O$	Methane	−0.24
$2CO_2 + 12H^+ + 12e^- = C_2H_4(g) + 4H_2O$	Ethene	−0.34
$CO_2 + 2H^+ + 2e^- = HCOOH(aq)$	Formic acid	−0.53
$CO_2 + 4H^+ + 4e^- = HCHO(aq) + H_2O$	Formaldehyde	−0.48
$CO_2 + 6H^+ + 6e^- = CH_3OH(aq) + H_2O$	Methanol	−0.38
$2CO_2 + 8H^+ + 8e^- = CH_3COOH(aq) + 2H_2O$	Acetic acid	−0.30
$2CO_2 + 10H^+ + 10e^- = CH_3CHO(aq) + 3H_2O$	Acetaldehyde	−0.35
$2CO_2 + 12H^+ + 12e^- = C_2H_5OH(aq) + 3H_2O$	Ethanol	−0.33
$3CO_2 + 16H^+ + 16e^- = C_2H_5CHO(aq) + 5H_2O$	Propionaldehyde	−0.32
$3CO_2 + 18H^+ + 18e^- = C_3H_7OH(aq) + 5H_2O$	Propanol	−0.31
$CO_2 + 4H^+ + 4e^- = C(s) + H_2O$	Solid carbon	−0.20

concentration. With the maturation of operating systems and the development of characterization techniques, the diversity of structures and intrinsic properties of MHPs have been explored, and their applications in environmental remediation and energy conversion have also received increasing research attention. In particular, photocatalytic CO_2 reduction is considered as the utmost promising strategy toward sustainable development with net zero carbon emission. According to numerous studies, the predominance of CO as the main MHP-based reduction product can be attributed to its two-electron transfer mode.[70,71] Moreover, CO is an important intermediate product in many chemical synthesis reactions and can be further converted into other organic compounds such as alcohols, ketones and acids.[72,73] Therefore, the production of CO by photocatalytic reduction based on MHPs will be discussed in this section with emphasis on the design strategies to improve the efficiency.

3.1 Lead-based MHPs for CO_2PR

In 2016, Park's team reported for the first time that an organic–inorganic mixed perovskite ($MAPbI_3$) could drive hydrogen evolution in aqueous hydrogen iodide solution and remain stable throughout the catalytic process.[74] As MHPs are unstable in polar solvents, ethyl acetate (EA) and acetonitrile (ACN) are generally considered as suitable media for the CO_2PR reaction.[8,52] Inspired by this, Xu *et al.* pioneered the synthesis of more stable $CsPbBr_3$ perovskite quantum dots ($CsPbBr_3$ QDs) in EA and successfully used them for photocatalytic CO_2 reduction (Fig. 5a).[52] However, the photocatalytic activity and durability of single-component $CsPbBr_3$ QDs are still low, which largely limits their further application. For this reason, they used a simple room-temperature antisolvent precipitation to synthesize a $CsPbBr_3$ QDs/GO composite, which exhibits a higher electron consumption rate of 29.8 μmol g^{-1} h^{-1} and the yield is much improved compared to $CsPbBr_3$ QDs (Fig. 5b).[52] Moreover, the $CsPbBr_3$ QDs/GO composite shows an enhanced photocurrent response (Fig. 5c) and reduced carrier transfer resistance (Fig. 5d), indicating the more favorable kinetics of the composite photocatalyst compared with $CsPbBr_3$ QDs. This study marks the first application of MHPs in CO_2 photoreduction, inspiring subsequent works on MHP-based materials for photocatalytic CO_2 reduction. To date, there have been many research works focusing on LHP-based composite photocatalysts, and the product is mainly CO with high selectivity (Table 2).

3.2 Lead-free MHP-based CO_2PR

For reasons of environmental considerations and safety issues, the development of green, non-polluting perovskites for CO_2 photoreduction is imperative, requiring partial or complete replacement of B-site Pb with atoms of similar radius, thus laying the groundwork for the development of CO_2PR in lead-free systems. It has been discovered that the remarkable photoelectric properties of Pb-based perovskite materials can be attributed to their unique electronic configuration, including lone-pair Pb $6s^2$ electrons and an empty Pb 6p orbital. Moreover, the substantial size and weight of Pb further strengthen these properties, contributing to a robust spin–orbit coupling effect, as elucidated by recent studies.[75,76] As such, in order to identify a stable and environmentally benign substitute for Pb, it is necessary to seek elements with similar atomic electronic configurations. Theoretically, the most suitable candidates for Pb replacement are group-14 metal elements, such as tin (Sn) and germanium (Ge), which also possess lone-pair s orbitals akin to Pb.[77,78] However, a major challenge arises as Sn- and Ge-based perovskites exhibit poor stability due to the rapid oxidation of Sn^{2+}/Ge^{2+} to Sn^{4+}/Ge^{4+}. Additionally, the potential toxicity of Sn to human beings upon environmental dispersion may surpass that of Pb, further complicating the quest for an ideal substitute. Hence, the pursuit of a stable and non-toxic Pb substitute demands meticulous investigation and consideration of various factors.

Recently, lead-free double perovskite $Cs_2AgBiBr_6$ has led to a research boom due to its non-toxicity, long carrier lifetime and high environmental stability. Taking advantage of these merits, $Cs_2AgBiBr_6$ has been adopted for NO removal,[79] degradation of organic pollutants,[67] H_2 evolution,[80–83] *etc.* Not long ago, $Cs_2AgBiBr_6$ was also explored for photocatalytic reduction of CO_2 and promising progress was made. For example, Zhou *et al.* developed novel lead-free double perovskite $Cs_2AgBiBr_6$

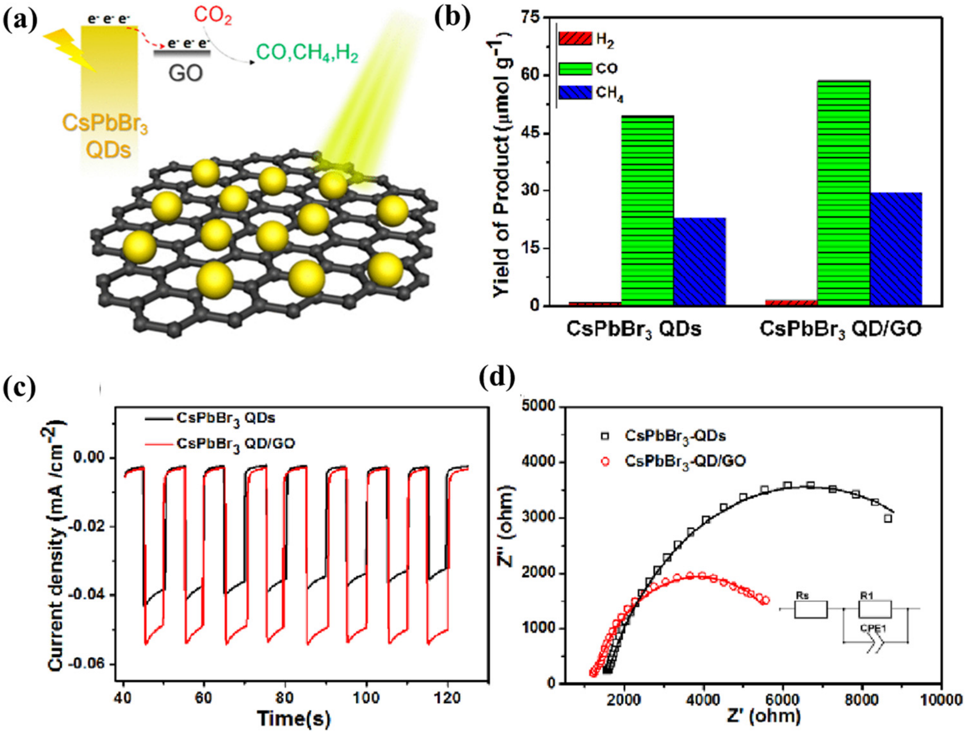

Fig. 5 (a) Photocatalytic performance: yield of the CO_2 reduction products after 12 h of photochemical reaction.[52] (b) UV-vis absorption spectra and the external quantum efficiency spectra.[52] (c) Amperometric I–t curves plotted at −0.4 V Ag/AgCl under chopped AM 1.5G illumination.[52] (d) EIS Nyquist plots recorded under 150-mW cm^{-2} illumination at a bias of −0.4 V Ag/AgCl; the lines are the corresponding fitted results. The inset is the equivalent circuit model.[52]

nanocrystals (NCs) for CO_2 photoreduction by thermal injection (Fig. 6a).[84] The corresponding crystal structure is shown in Fig. 6b, where Ag^+ and Bi^{3+} ions located at the B and B′ sites combine with Br^- to replace the conventional Pb^{2+}, forming two types of regular octahedra. These two octahedra alternately join to form a rock salt face-centred cubic structure, with the larger Cs^+ filling their gaps to form the typical $A_2BB'X_6$ structure. Photocatalytic CO_2 reduction was carried out in EAC in a Pyrex glass bottle under simulated sunlight (AM 1.5G, 150 mW cm^{-2}) irradiation. Both as-prepared and washed NCs were tested and the photocatalytic performance is displayed in Fig. 6c. After 6 h of continuous irradiation, the CO and CH_4 yields are 5.5 and 0.65 μmol g^{-1}, respectively, using $Cs_2AgBiBr_6$ NCs without an additional washing process. Fig. 6d presents a preliminary mechanism for the photocatalytic reduction of CO_2 by $Cs_2AgBiBr_6$ NCs, where $Cs_2AgBiBr_6$ NCs have a suitable conduction band to drive CO_2 reduction. This is the first example of the successful application of double perovskites for CO_2 photoreduction. Based on the above research, scholars began to consider optimizing the dimensions to improve the performance of $Cs_2AgBiBr_6$. Very recently, Liu *et al.* fabricated two-dimensional $Cs_2AgBiBr_6$ nanoplatelets (NPLs) and found that $Cs_2AgBiBr_6$ NPLs exhibit stronger photocatalytic performance than the corresponding nanocubes (NCs), which was explained by the long in-plane diffusion length and anisotropic charge carryover of the NPLs, as compared to their NC counterparts (Fig. 6e).[85] Fig. 6f depicts the reaction mechanism of 2D $Cs_2AgBiBr_6$ NPLs, which is similar to that of 0D $Cs_2AgBiBr_6$ NCs, in which photogenerated charge carriers (electrons and holes) dissociate in the NPLs, with the holes subsequently consumed by solvent molecules and the electrons trapped by CO_2. As shown in Fig. 6g, the production rates of both CO and CH_4 are significantly higher when NPLs are utilized as catalysts. However, as the reaction time increases, the production rate gradually decreases, which is probably due to the surface poisoning of some surfaces of the photocatalysts. The overall electron consumption of $Cs_2AgBiBr_6$ NPLs during the reaction increases by more than 8 times compared to $Cs_2AgBiBr_6$ NCs (255.4 μmol g^{-1} *vs.* 30.8 μmol g^{-1} in Fig. 6h). However, due to their inherent indirect bandgap, the single-component Bi-based perovskites show insufficient photocatalytic activity in practical applications.

Encouragingly, recent studies on catalyst growth and optimization of interfacial reactions/conditions are expected to lead to the further development of Bi-based perovskites. Furthermore, by compounding with other materials, building a two-component composite catalyst results in enhanced photocatalytic activity and stability. For instance, Ding's group reported an *in situ* assembly approach to produce a stable $Cs_2AgBiBr_6$/Ce-UiO-66-H composite, in which a tight contact interface is constructed between the two involved components.[45] As shown in Fig. 6i, benefiting from the photocatalytic properties and the high adsorption capacity for CO_2, the optimized 20$Cs_2AgBiBr_6$/Ce-UiO-66-H adsorption-photocatalyst shows

Table 2 LHP-based catalysts for CO_2PR with CO-dominated products

Photocatalyst	Light source	System	$R_{\text{total electron}}$ (μmol g^{-1} h^{-1})	Products	Selectivity (%)	Ref.
$CsPbBr_3$ QDs	100 W Xe-lamp, AM 1.5G	EA	23.7	CO, CH_4, H_2	99.3	37
$CsPbBr_3$/BP	200 W Xe-lamp	EA/H_2O	174.7	CO, CH_4	~100	54
$Co_{2\%}$@$CsPbBr_3$/Cs_4PbBr_6	—	H_2O	27.1	CO, CH_4	~100	55
$CsPbBr_3$ NC/Pd NS	150 W Xe-lamp, $\lambda > 420$ nm	H_2O (vapor)	33.79	CO, CH_4, H_2	94.8	96
$CsPbBr_3$–Au	100 W Xe-lamp, $\lambda > 420$ nm	ACN/IPA	47.7	CO, CH_4	~100	98
3DOM Au–$CsPbBr_3$	—	IPA/H_2O/EA	38.0	CO, CH_4	~100	99
$CsPbBr_3$–Re(600)	—	TL/IPA	73.34	CO, H_2	95	101
$CsPbBr_3$–Ni(tpy)	—	EA/H_2O	1252	CO, CH_4	~100	102
Mn:$CsPb(Br/Cl)_3$	—	EA	498.9	CO, CH_4	~100	106
Non-cube $CsPbBr_3$	450 W Xe-lamp	EA/H_2O	182.95	CO, CH_4	~100	107
$CsPbBr_3$–OA/OAm	—	H_2O (vapor)	9.6	CO	~100	112
$CsPbBr_3$–glycine	—	H_2O (vapor)	55.4	CO	~100	112
$CsPbBr_3$QDs/UiO-66(NH_2)	300 W Xe lamp, $\lambda > 420$ nm	EA/H_2O	101.65	CO, CH_4	~100	115
TiO_2/$CsPbBr_3$	300 W Xe-lamp (UV-vis light)	ACN/H_2O	<18.99	CO, H_2	95	118
$CsPbBr_3$ QDs/Bi_2WO_6	—	EA/H_2O	114.4	CO, CH_4	~100	121
$(ha)_2CsPb_2Br_7$	300 W Xe-lamp, full wavelength	BAC	377.58	CO, CH_4	~100	161
$CsPbBr_3$/FLG	Laser diode λ = 405 nm	EA	255.4	CO, CH_4, H_2	>99	162
$CsPbBr_3$–BF_4/Co	—	EA/IPA	180	CO, CH_4	~100	163
$CsPbBr_3$	150 W Xe-lamp, $\lambda > 380$ nm	EA	2.7	CO, CH_4, H_2	95.2	164
$CsPbBr_3$/Pt	150 W Xe-lamp, $\lambda > 380$ nm	EA	5.6	CO, CH_4, H_2	90.56	164
$CsPbBr_3$/$Ti_3C_2T_x$ MXene	300 W Xe-lamp, $\lambda > 400$ nm	H_2O (vapor)	112.6	CO, CH_4	~100	165
$CsPbBr_3$	300 W Xe-lamp, AM 1.5G	EA/H_2O	20.9	CO, CH_4, H_2	>99	166
$CsPbBr_3$/CTF-1	—	EA	96.4	CO	~100	167
$CsPbBr_3$/CTF-1-Ni	—	EA	173	CO	~100	167
$CsPbBr_3$ NC/Pd NS	150 W Xe-lamp, $\lambda > 420$ nm	H_2O (vapor)	33.79	CO, CH_4, H_2	94.8	168
WO_3/$CsPbBr_3$/ZIF-67	—	H_2O (vapor)	~66.25	CO	~100	169
$CsPbBr_3$/WO_3	300 W Xe-lamp, $\lambda > 400$ nm	EA/H_2O	~400	CO	~100	170
$CsPbBr_3$/MoS_2	—	EA/H_2O	152.4	CO, CH_4	~100	171
P3HT/$CsPbBr_3$	—	ACN/H_2O	475.3	CO, CH_4	~100	172
$CsPbBr_3$@$GDY_{0.3}$	—	ACN/H_2O	20.4	CO	~100	173
$CsPbBr_3$@$GDY_{0.3}$–Co	—	ACN/H_2O	55.4	CO	~100	173
C_{60}/$CsPbBr_3$	—	ACN/H_2O	90.2	CO, CH_4	~100	174
$CsPbBr_3$@SnO_2	300 W Xe-lamp	EA/H_2O	128.2	CO, CH_4	~100	175
$CsPbBr_3$/AgBr	—	ACN/H_2O	141.1	CO, CH_4	~100	176
$CsPbBr_3$/BiOBr	—	EA/H_2O	72.3	CO, CH_4	~100	177
MIL-100(Fe)–$CsPbBr_3$	—	H_2O (vapor)	82	CO, CH_4	~100	178
0D $CsPbBr_3$/2D $CsPb_2Br_5$	—	H_2O (vapor)	400.62	CO, CH_4	~100	179
NMF/$CsPbBr_3$-NWs	300 W Xe-lamp, $\lambda > 420$ nm	EA/H_2O	162	CO	~100	180
$CsPbBr_3$ PQDs/PbS	—	EA/H_2O	73.1	CO, CH_4, H_2	>99	181
Mn:$CsPbCl_3$	—	—	74	CO	~100	182
$CsPbBr_3$@MTB	300 W Xe-lamp	EA/H_2O	145.28	CO, CH_4, H_2	>99	183
$CsPbBr_3$/BiOCl	300 W Xe-lamp	EA/H_2O	97.2	CO, CH_4	~100	184
$CsPbBr_3$/CoAl-LDH	300 W Xe lamp, $\lambda > 420$ nm	EA/H_2O	41.2	CO, CH_4	~100	185
$CsPbBr_3$/NCP	300 W Xe lamp, $\lambda > 420$ nm	EA/H_2O	77.6	CO, CH_4	~100	186
T-$SrTiO_3$/$CsPbBr_3$	—	H_2O (vapor)	~120.2	CO	~100	187
Pb-rich Ni:$CsPbCl_3$ NCs	—	H_2O (vapor)	339.4	CO, CH_4	~100	188
$CsPbBr_3$/PbSe	—	EA/H_2O/IPA	322.4	CO	~100	189
$CsPbBr_3$ QDs/BP NSs	—	H_2O (vapor)	76.6	CO	~100	190
MWCNT/$CsPbBr_3$	—	ACN/H_2O	32.96	CO, CH_4	~100	191
$CsPbBr_3$@Cu-TCPP	300 W Xe lamp, $\lambda > 420$ nm	ACN/H_2O	150.04	CO, CH_4	~100	192
Cs_4PbBr_6/rGO	300 W Xe lamp, $\lambda > 420$ nm	EA/H_2O	11.4	CO, CH_4	~100	193
$SrTiO_3$/$CsPbBr_3$	300 W Xe lamp	H_2O (vapor)	~240.4	CO	~100	194
$CsPbBr_3$/USGO/a-Fe_2O_3	—	ACN/H_2O	147.6	CO	~100	195
$CsPbBr_3$ NCs/MXene-20	—	EA	110.64	CO, CH_4	~100	196

excellent performance in CO_2 reduction with a rather high CO production rate (309. 01 μmol g^{-1} h^{-1}), which is 2.1 and 2.7 times higher than that of pure $Cs_2AgBiBr_6$ and Ce-UiO-66-H respectively. The excellent photocatalytic conversion of CO_2 is attributed to the efficient solar energy harvesting and fast photoexcited carrier separation in the assembled structure. Importantly, due to the *in situ* synthesis, $Cs_2AgBiBr_6$ QDs are intercalated in the Ce-UiO-66-H framework, which leads to better stability and induces a large number of oxygen vacancies in $Cs_2AgBiBr_6$/Ce-UiO-66-H, maintaining a constant CO_2 conversion during a continuous 10 h cycling test in wet air (illustrated in Fig. 6j). In addition, Feng's group constructed a Type-Z heterojunction composed of $Cs_3Bi_2I_9$ nanosheets and CeO_2 nanosheets ($Cs_3Bi_2I_9$/CeO_2-3:1) as a photocatalyst for CO_2 photoreduction and H_2O oxidation using an electrostatic self-assembly strategy (Fig. 6k).[86] Owing to the well-matched energy levels and tight interfacial contacts, the separation efficiency of photogenerated carriers in the $Cs_3Bi_2I_9$/CeO_2-3:1 composite is significantly improved. The $Cs_3Bi_2I_9$/CeO_2-3:1 composite catalyst shows a high photocatalytic activity in the reduction

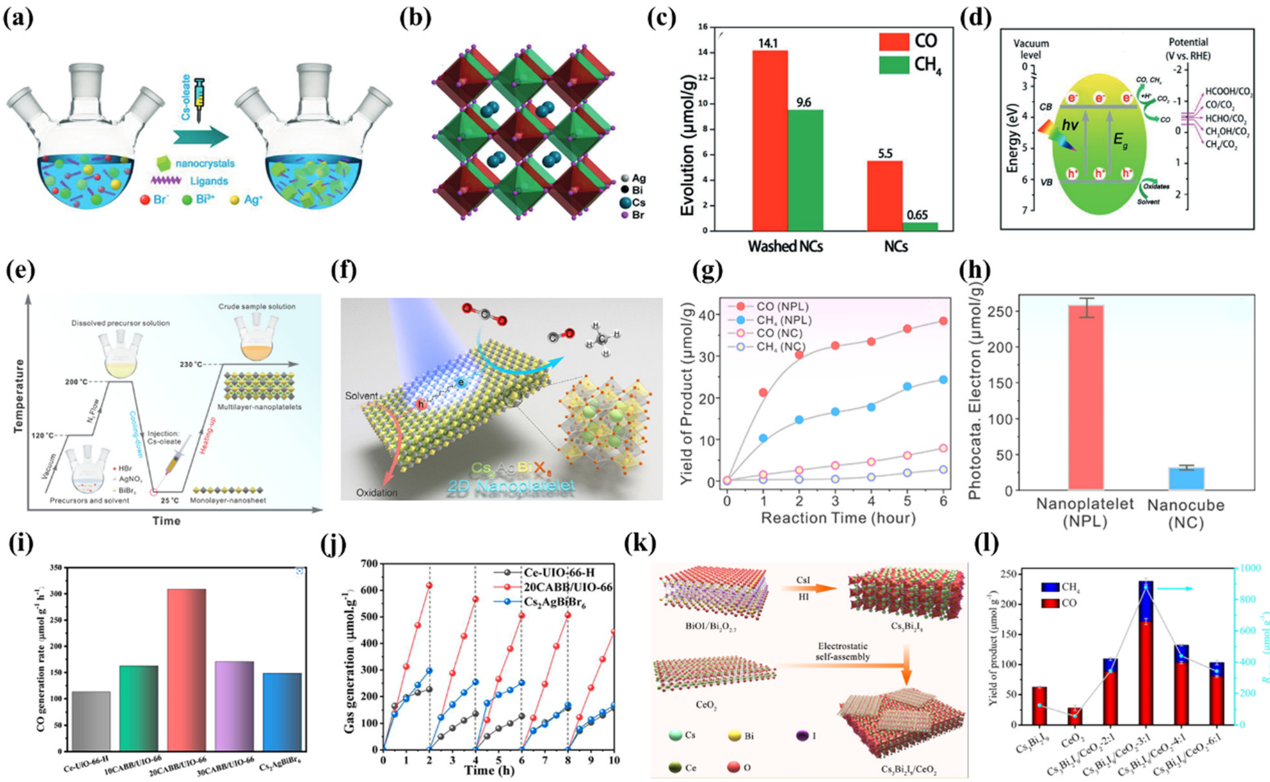

Fig. 6 (a) Schematic illustration of the solution phase synthesis of $Cs_2AgBiBr_6$ NCs (hot-injection route).[84] (b) Crystal structure of cubic $Cs_2AgBiBr_6$.[84] (c) Comparison of the photocatalytic CO_2 reduction performance of the as-prepared $Cs_2AgBiBr_6$ NCs and washed NCs.[84] (d) Schematic diagram of the photoreduction of CO_2 on the surface of $Cs_2AgBiBr_6$ NCs.[84] (e) Schematic illustration of the synthetic procedure of lead-free Cs_2AgBiB_{r6} double perovskite 2D NPLs.[85] (f) Schematic illustration of the $Cs_2AgBiBr_6$ NPL photocatalyzed CO_2 reduction reaction.[85] (g) CO (red) and CH_4 (blue) product yield evolution as a function of reaction time using $Cs_2AgBiBr_6$ double perovskite NPLs (solid) and NCs (open) as catalysts.[85] (h) Histogram of the total photocatalytic electron consumption in 6 h for the reactions using $Cs_2AgBiBr_6$ double perovskite NPLs (red) and NCs (blue) as catalysts.[85] (i) CO generation rate during CO_2 reduction under 300 W Xe lamp irradiation with as-prepared samples.[45] (j) The recycling test for the photocatalytic activity of Ce-UiO-66-H, 20CABB/UiO-66, and $Cs_2AgBiBr_6$.[45] (k) The preparation of $Cs_3Bi_2I_9$ nanosheets and the self-assembly between $Cs_3Bi_2I_9$ and CeO_2 nanosheets.[86] (l) The yields of CO and CH_4 over $Cs_3Bi_2I_9$, CeO_2 and $Cs_3Bi_2I_9/CeO_2$-x:1 (x = 2–6) in 12 h.[86]

of CO_2 to CO/CH_4 with an electron consumption yield of 877.04 μmol g^{-1}, which is 7 and 15 times higher than the yields of pristine $Cs_3Bi_2I_9$ and CeO_2 nanosheets (Fig. 6l). This work exceeds the yields of other currently reported Bi-based perovskites in photocatalytic CO_2 reduction.

Overall, MHPs have shown promising results in photocatalytic CO_2 reduction to CO due to their high light absorption and efficient charge transfer properties. Particularly, lead-based perovskites have been extensively studied in this area and have achieved favorable conversion efficiencies. However, the toxicity of lead and concerns over stability have led to increased interest in lead-free alternatives. Lead-free perovskites such as Sn-based, Bi-based, and mixed-metal perovskites have been investigated for CO_2 reduction and especially Bi-based perovskites have shown comparable or even superior performance to lead-based perovskites. Nonetheless, challenges such as instability under operating conditions and limited understanding of reaction mechanisms remain as major obstacles to their commercial viability. For this reason, the next section will focus on the strategies to improve the photoconversion efficiency and stability of MHP-based photocatalysts, with the purpose of bringing some enlightenment to the development of stable and efficient catalytic systems (Table 3).

3.3 Strategies to improve the photo-conversion performance of MHPs

3.3.1 Morphological regulation. Perovskites have many different morphologies, such as 0D QDs, 1D rods, 2D nanosheets, 3D cube/star-shaped nanocrystals, *etc.*, which can significantly affect the CO_2 reduction performance. Sun *et al.* reported a variety of shapes of $CsPbX_3$ materials prepared by a facile ligand-assisted method and found that $CsPbX_3$ materials exhibit shape-dependent photoelectronic properties.[87] For example, the extremely small particle size of $CsPbBr_3$ QDs makes it significantly different from bulk materials in terms of optical and electronic properties. These 0D $CsPbBr_3$ QDs can be easily functionalized *via* surface modification, with tunable luminescence wavelength when they are in solution and their forbidden bandwidth becomes narrower when they grow in aggregation (Fig. 7a). Similarly, a relevant report has demonstrated that the quantum dots are better than conventional fluorescent organic dyes in terms of tunable broad excitation

Table 3 Lead-free MHP-based catalysts for CO_2PR with CO-dominated products

Photocatalyst	Light source	System	$R_{\text{total electron}}$ (μmol g^{-1} h^{-1})	Products	Selectivity (%)	Ref.
$Cs_3Bi_2I_9/Bi_2WO_6$	—	H_2O (vapor)	14.67	CO	~100	42
$Cs_3Bi_2Br_9$	—	H_2O (vapor)	54.6	CO, H_2	98.7	43
$Cs_2AgInCl_6$@Ag-2	300 W Xe lamp	EA	71	CO, CH_4	~100	44
$Cs_2AgBiBr_6$/Ce-UiO-66-H	—	H_2O (vapor)	623.7	CO	~100	45
$Cs_2AgBiBr_6/Sr_2FeNbO_6$	—	EA/H_2O	164.96	CO, CH_4	~100	46
Cs_2CuBr_4	—	H_2O (vapor)	179.29	CO, CH_4	~100	47
Cs_2CuBr_4@KIT-6	300 W Xe lamp	EA/H_2O	240.5	CO, CH_4	~100	66
$Cs_2AgBiBr_6$	—	EA	17.5	CO, CH_4	~100	84
$Cs_3Bi_2I_9/CeO_2$-3:1	—	H_2O (vapor)	877.04	CO, CH_4	~100	86
$Cs_3Bi_2I_9$			7.3	CO	~100	92
$Cs_3Bi_2(Cl_{0.5}Br_{0.5})_9$	—	H_2O (vapor)	32	CO	~100	92
3D $Cs_2NaBiCl_6$	300 W Xe lamp	H_2O (vapor)	69.4	CO	~100	93
Cs_2CuBr_4/CeO_2	300 W Xe lamp	EA/H_2O	241.82	CO, CH_4	~100	100
MCM-41@$Cs_3Bi_2Br_9$	—	H_2O (vapor)	34.48	CO	~100	109
$Cs_2AgBiBr_6$@MCM-48	300 W Xe lamp, $\lambda > 420$ nm	EA	99.13	CO, CH_4	~100	110
ZnSe–$CsSnCl_3$	—	TL/IPA	128.32	CO, CH_4	~100	114
$Cs_2AgBiBr_6$/CTF-1	300 W Xe lamp, $\lambda \geq 420$ nm	EA	130.2	CO, CH_4	~100	127
$Cs_4CuSb_2Cl_{12}$	300 W Xe lamp	H_2O (vapor)	351	CO, CH_4	~100	197
$Cs_3Sb_2Br_9$	—	ODE/H_2O	255	CO	~100	198
$Rb_3Bi_2I_9$	32 W UV-lamp, $\lambda = 305$ nm	H_2O (vapor)	17.24	CO, CH_4	~100	199
$MA_3Bi_2I_9$	—	—	9.28	CO, CH_4	~100	199
CABB/Ni-MOF	300 W Xe lamp	EA	241.14	CO, CH_4	~100	200
$Cs_2AgBiBr_6/Bi_2WO_6$	300 W Xe lamp, $\lambda > 420$ nm	EA/IPA	87.66	CO, CH_4	~100	201
$Cs_3Sb_2I_9$	—	H_2O (vapor)	95.7	CO	~100	202
$Cs_2AgBiBr_6/Ti_3C_2T_x$	150 W Xe-lamp, $\lambda \geq 400$ nm	H_2O (vapor)	50.6	CO, CH_4, H_2	—	203
$Cs_3Bi_2Br_9$/MOF 525 Co	300 W Xe lamp	H_2O (vapor)	124.8	CO, CH_4	~100	204
$Cs_3Sb_2(Br_{0.7}I_{0.3})_9$	—	H_2O (vapor)	18.5	CO	~100	205
Cs_2TeCl_6	300 W Xe lamp	H_2O (vapor)	320	CO, CH_4	~100	206
Cs_2TeBr_6	300 W Xe lamp	H_2O (vapor)	366.8	CO, CH_4	~100	207
$Cs_2AgBiBr_6@SiO_2$	$\lambda > 420$ nm	ACN/H_2O	271.76	CO, H_2	93.8	208
$Cs_2AgBiBr_6$–Cu–RGO	—	H_2O (vapor)	91.4	CO, CH_4, H_2	97.8	209

and narrow emission spectra, signal brightness, high quantum yields and photostability.[88] One of the properties of 2D materials is the large exciton binding energy due to dielectric shielding and reduced quantum confinement effects.[89] For example, the exciton binding energy of monolayer WS_2 is as high as 700 MeV. 2D halide perovskites have significant vibrational intensity, large exciton binding energy, effective radiative recombination and high photoluminescence quantum yields, which result from the large energy difference and high dielectric constant between the inorganic and organic layers.[90] Moreover, the exciton binding energy of two-dimensional perovskites can be fine-tuned by inserting small molecular layers.[91] In a study conducted by Wu *et al.*, 2D $CsPbBr_3$ nanosheets were synthesized at room temperature by varying the amount of hydrobromic acid employed in the synthesis process (as depicted in Fig. 7b), resulting in nanosheets with thicknesses of 2, 3, 4, and 4.6 nm.[92] The effect of $CsPbBr_3$ nanosheet thickness was investigated for photocatalytic CO_2 reduction in water vapor and CO_2 gas (gas–solid system without a sacrificial agent). It was found that the thickness of $CsPbBr_3$ nanosheets has a significant effect on the performance of CO_2 photoreduction, and the CO generation rates of 2.3, 14.2, 21.6, 12.5 and 5.7 μmol g^{-1} h^{-1} are observed for 2, 3, 4 and 4.6 nm thick $CsPbBr_3$ nanosheets and nanocrystal $CsPbBr_3$, respectively (Fig. 7c and d). Among these, $CsPbBr_3$ nanosheets with a thickness of 4 nm exhibit the highest photocatalytic activity, which can be attributed to the suitable visible light absorption range and the higher number of photogenerated carriers for CO_2 reduction. From another perspective, the 2D $CsPbBr_3$ nanosheets have shorter carrier transfer distances and uncoordinated active metal sites compared to the bulk $CsPbBr_3$ nanocrystals, favoring the transport of photogenerated carriers to the catalyst surface. In a study by Pi and his collaborators, they prepared chlorine-deficient 3D-graded $Cs_2NaBiCl_6$ porous microspheres assembled from highly crystalline nanosheets by a grinding method (Fig. 7e).[93] The CO yield of gas–solid photocatalytic reduction of CO_2 in the absence of sacrificial agents reached 30.22 μmol g^{-1} h^{-1}. Experimental results and density functional theory (DFT) calculations indicate that the chlorine vacancies possess the triple effect of inhibiting photogenerated electron–hole complexation, enhancing CO_2 adsorption, and significantly reducing the free energy barrier for the generation of the key intermediate COOH*. Moreover, the surface and defect engineering coupling of the 3D hierarchical sample brings a 12.34-fold enhancement of CO_2 photoreduction activity compared to the pristine $Cs_2NaBiCl_6$ (Fig. 7f).

3.3.2 Co-catalyst modification. When used on their own, co-catalysts have little or no activity. When used as an additive to the primary catalyst, the addition of co-catalysts can change the catalyst surface structure, the distribution of pore structure, the valence of ions, acidity and alkalinity, *etc.*, which can improve the overall activity, stability, selectivity and lifetime of the catalyst. In photocatalytic reactions, the rate of charge separation is one of the critical factors determining the overall efficiency. Utilizing co-catalysts to improve the photoconversion efficiency has been reported as an effective strategy in

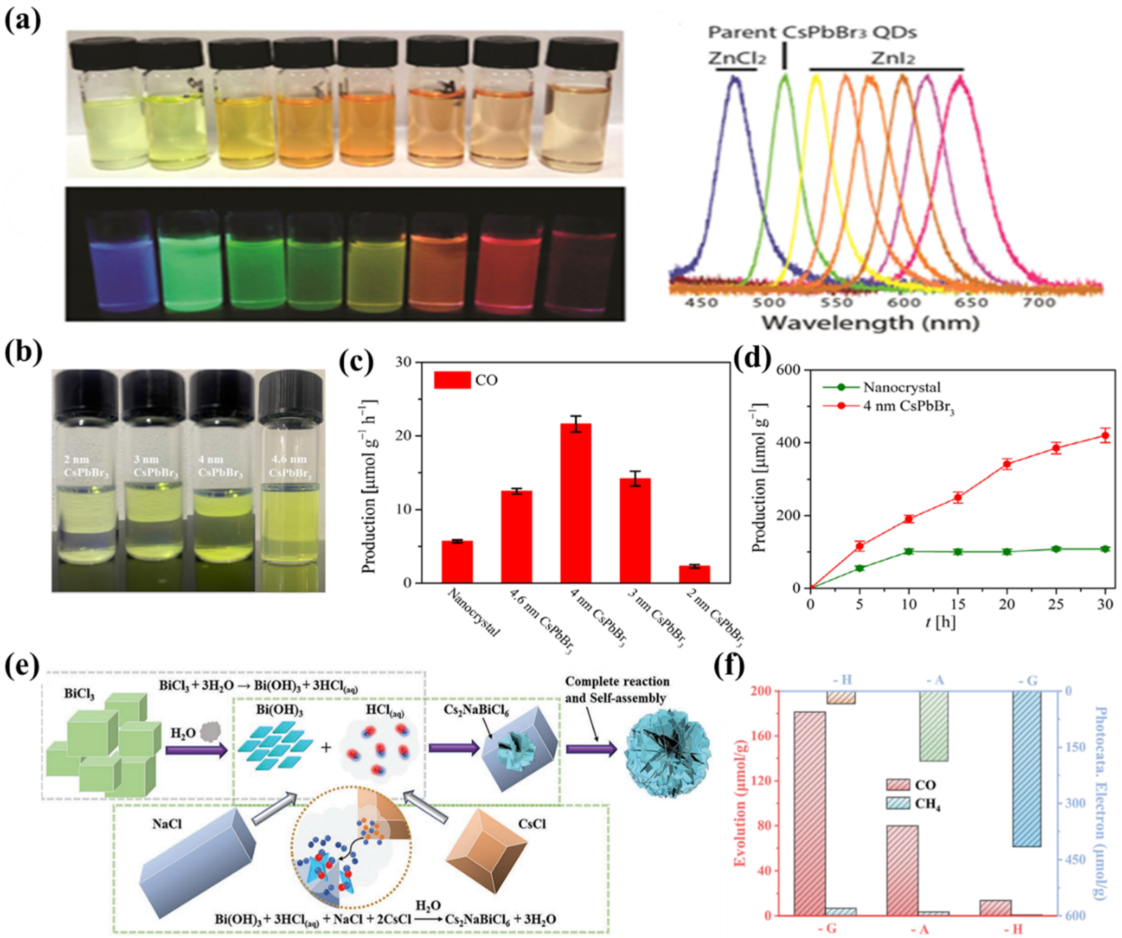

Fig. 7 (a) Anion exchange of the as-synthesized spherical $CsPbBr_3$ quantum dots with stable dispersions in toluene under room light or excitation using an ultraviolet lamp at room temperature and PL spectra of the solutions.[87] (b) Photographic images of $CsPbBr_3$ nanosheets exposed to sunlight (top) and an ultraviolet lamp (bottom) in hexane.[92] (c) The comparison of CO production with $CsPbBr_3$ NCs and $CsPbBr_3$ nanosheets as photocatalysts after 5 h of irradiation under a 300 W Xe lamp, with a light intensity of 100 mW cm^2.[92] (d) Photocatalytic evolution of CO catalyzed by $CsPbBr_3$ NCs and 4 nm $CsPbBr_3$ nanosheets in the CO_2 and water vapor system.[92] (e) A feasible growth diagram of three-dimensional hierarchical structure $Cs_2NaBiCl_6$-G.[93] (f) CH_4 and CO generation from CO_2 photoreduction using different star nanocrystals.[93]

previous studies.[94,95] Specifically, the roles played by co-catalysts in the photoreduction process include the following: (1) promoting the separation of photogenerated electron–hole pairs; (2) reducing the overpotential required for CO_2 reduction; (3) improving the overall catalyst stability; and (4) enhancing the selectivity of CO_2 and hindering other side reactions. In order to better describe the roles of co-catalysts, several typical co-catalytic reaction systems are described later.

3.3.2.1 Noble metal deposition. Most semiconductors require additional catalysts to achieve high CO_2 reduction activity, even in the presence of a sacrificial electron donor. This is caused by both the tendency of electron–hole pairs to recombine before reaching the surface for reaction and the slow surface reaction that does not allow efficient charge consumption. With the purpose of extracting electrons to the surface, metals such as platinum are traditionally used as co-catalysts. Noble metals, in particular, act as electron sinks and provide effective proton reduction sites that greatly enhance the proton reduction reaction. Of these, Pd and Pt are widely used as typical noble metal co-catalysts for photocatalytic reactions. As an example, Kuang' s group prepared a novel 0D $CsPbBr_3$ nanocrystal/2D Pd nanosheet composite photocatalyst that can catalyze CO_2 conversion efficiently and stably under visible light irradiation (Fig. 8a).[96] The enhanced photocatalytic activity can be explained by the Pd nanosheets acting as an electron reservoir, rapidly separating electron–hole pairs in the $CsPbBr_3$ nanocrystals *via* Schottky contacts and providing ideal sites for the CO_2 reduction reaction. The highest electron consumption rate of the $CsPbBr_3$ nanocrystal/Pd nanosheet composite is 33.79 μmol g^{-1} h^{-1}, which is 2.43 times higher than that of the pristine $CsPbBr_3$ nanocrystal (9.86 μmol g^{-1} h^{-1}), providing a practical and versatile solution to enhance the photocatalytic performance of MHPs through semiconductor/metal design (Fig. 8b). Meanwhile, their team also reported $CsPbBr_3$ as a photocatalyst for CO_2 reduction with high stability and selectivity in non-aqueous solvents.[97] In view of the crucial role of solvents in enhancing the photocatalytic reaction rate, EA was chosen as the most effective solvent. Besides, the

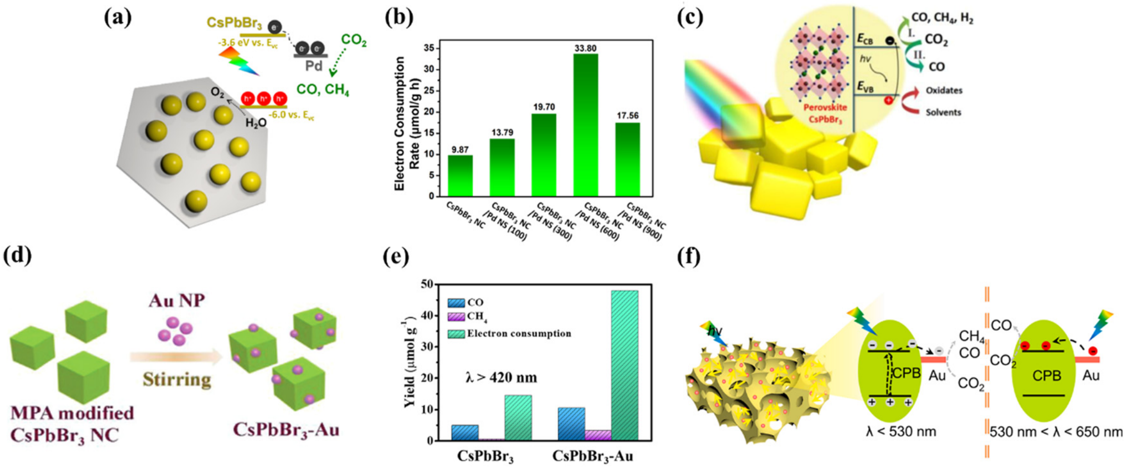

Fig. 8 (a) The sketch of the composite material and its corresponding band alignments.[96] (b) The electron consumption rates under visible light illumination (>420 nm).[96] (c) Schematic diagram of the photoreduction of CO_2 on the surface of $CsPbBr_3$ crystals with (I) and without (II) the participation of protons.[97] (d) Sketch of the fabrication of $CsPbBr_3$–Au nanocomposites; morphology characterization of the synthesized $CsPbBr_3$–Au nanocomposite.[98] (e) Photocatalytic performance: yield of the CO_2 reduction products and electron consumption over $CsPbBr_3$ and $CsPbBr_3$–Au under illumination with $\lambda > 420$ nm.[98] (f) The possible charge transfer route during the photocatalytic reaction.[99]

addition of a Pt co-catalyst by photochemical deposition further improves the electron yield, highlighting the importance of optimizing the reaction medium and surface catalytic activity for superior performance (Fig. 8c). In addition to Pd and Pt, the loading of Au as a co-catalyst on the inner/outer surface also facilitates the efficient conversion of CO_2 to CO. Recently, Liao and co-workers explored a novel photocatalyst ($CsPbBr_3$–Au), which has the ability to excite wavelength-dependent photocatalytic reduction of CO_2 (Fig. 8d).[98] Under visible light ($\lambda > 420$ nm) illumination, photogenerated electrons in $CsPbBr_3$ are available for injection into Au with an electron injection rate and efficiency of 2.84×10^9 s^{-1} and 78%, respectively. The enhanced charge separation further translates into 3.2-fold enhancement in photocatalytic CO_2 reduction activity compared to pristine $CsPbBr_3$ (Fig. 8e). Experimental results indicate that the nanocomposite has a strong local surface plasmon resonance effect in the visible region and can effectively promote the CO_2 reduction reaction. Not too long ago, Huang *et al.* demonstrated a three-dimensionally ordered macroporous Au–$CsPbBr_3$ (3DOM Au–CPB) composite loaded with gold nanoparticles, achieving better carrier separation performance through band bending effects at the Au/CPB interface (Fig. 8f).[99] As for Bi-based perovskites, Au loading also enhances the CO_2 photoreduction efficiency. For example, Fu *et al.* prepared a $Cs_3Bi_2Br_9/V_2O_5$ photocatalyst that reduced CO_2 to CO with a yield of 37.8 μmol g^{-1} h^{-1}, which is 5.3 times higher than that of pure $Cs_3Bi_2Br_9$.[100] In addition, the loading of Au nanoparticles on $Cs_3Bi_2Br_9/V_2O_5$ as a co-catalyst further improves the separation efficiency of the photogenerated charge carriers. The optimum Au–$Cs_3Bi_2Br_9/V_2O_5$ composite exhibits a high CO yield of 98.95 μmol g^{-1} h^{-1} with a selectivity of 98.74%.

3.3.2.2 Molecular immobilization. Chen *et al.* designed a novel $CsPbBr_3$–Re(CO)$_3$Br(dcbpy) (dcbpy = 4,4′-dicarboxy-2,2′-bipyridine) complex photocatalyst by immobilizing the molecule on the surface of $CsPbBr_3$ nanocrystals as a co-catalyst (Fig. 9a).[101] Due to the strong interfacial interactions, an efficient extraction of electrons from $CsPbBr_3$ to the complex molecule can be established, which allows an enhanced synergistic interaction with each other to obtain visible light-driven catalytic activity and product selectivity. The optimized $CsPbBr_3$–Re(600) sample yields a high R_{electron} of 73.34 μmol g^{-1} h^{-1}, which is approximately 23 times higher than that of the pristine $CsPbBr_3$ (Fig. 9b). In addition, the composite catalyst exhibited good catalytic stability, with a CO yield of 509.14 μmol g^{-1} after 15 h of continuous illumination (Fig. 9c). Another study has also demonstrated the significant effect of molecular anchoring in promoting efficient CO_2 photoconversion. Wang and co-workers immobilized $[Ni(terpy)_2]^{2+}$(Ni(tpy)) on the inorganic ligand-capped $CsPbBr_3$ NC and utilized the hybrid as a visible-light-driven CO_2 reduction catalyst (Fig. 9d).[102] In this hybrid photocatalytic system, Ni(tpy) can provide a specific catalytic site and act as an electron absorber to inhibit electron–hole radiation in the $CsPbBr_3$ NC. The $CsPbBr_3$–Ni(tpy) catalytic system achieves a high yield (1724 μmol g^{-1}) for the reduction of CO_2 to CO/CH_4, which is about 26-fold higher than that of the pristine $CsPbBr_3$ NCs and R_{electron} as high as 1252 μmol g^{-1} h^{-1} (Fig. 9e). Notably, this work shows the highest performance of lead-based perovskites for CO_2PR to date.

3.3.3 Ion doping. Doping is considered as an effective and facile method to improve the catalytic performance of photocatalysts.[103] By doping and substituting heterogeneous cations in LHPs, their overall photoelectric performance can be significantly improved.[104] Recently, Tang *et al.* used DFT calculations to predict that when Co and Fe atoms are doped into the perovskite, its catalytic capacity for CO_2 reduction will increase.[105] The basis is in the case of Co and Fe doping, the perovskite adsorbs CO_2*, C*OOH and HCOO* intermediates much more strongly than the pristine perovskite (Fig. 10a).

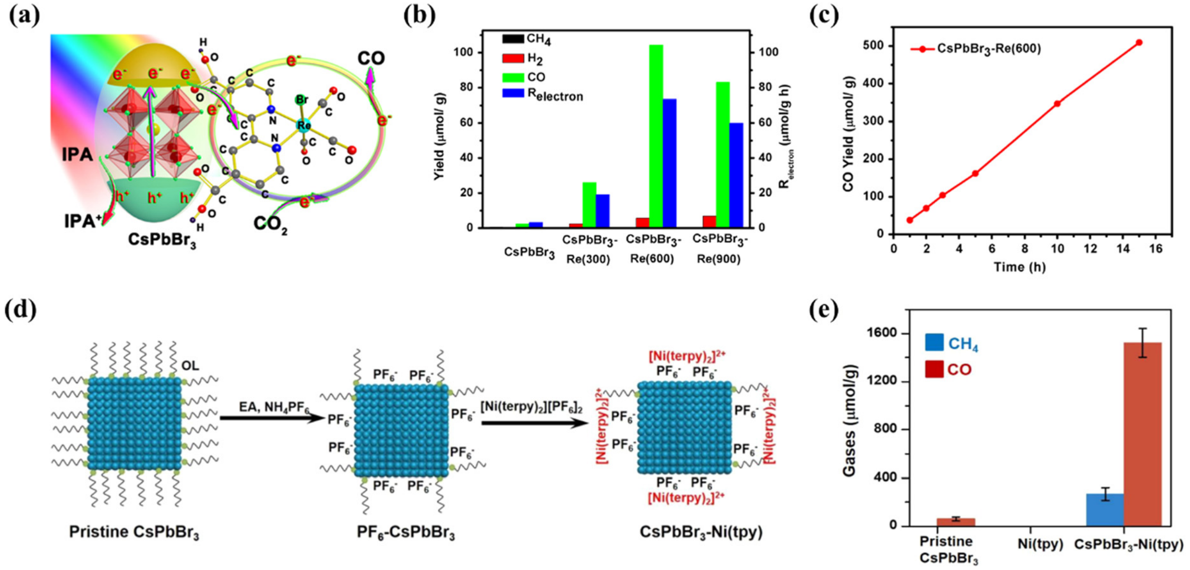

Fig. 9 (a) Schematic diagram of the working principle of the $CsPbBr_3$–$Re(CO)_3Br(dcbpy)$ composite in CO_2 reduction.[101] (b) Photocatalytic CO_2 reduction performances: product yield after 3 h of reaction.[101] (c) Time course of CO yield of $CsPbBr_3$–Re(600) during 15 h of continuous illumination.[101] (d) Schematic of the formation of the $CsPbBr_3$–Ni(tpy) photocatalyst.[102] (e) Production of gases using various photocatalysts based on pristine $CsPbBr_3$, pristine Ni(tpy) and $CsPbBr_3$–Ni(tpy); error bars correspond to standard deviations based on three experiments.[102]

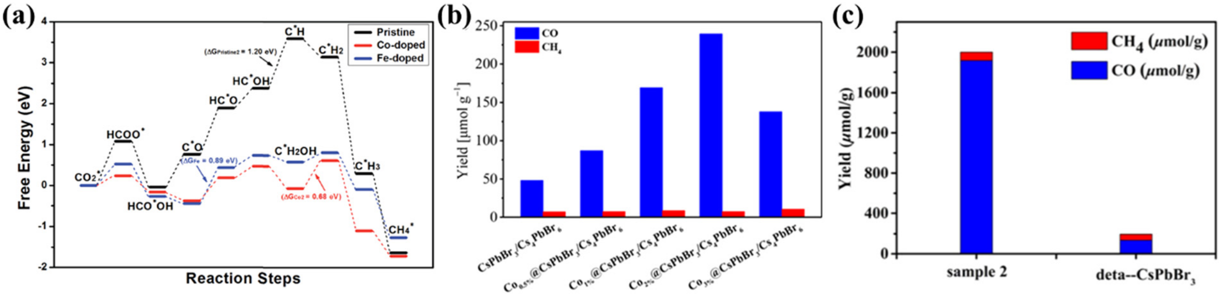

Fig. 10 (a) The free energy diagrams of the most favored paths of CO_2 reduction in pristine, Co-doped and Fe-doped cases. The DG of the rate-determining step for each case is listed.[105] (b) The yields of CO and CH_4 generated from photocatalytic CO_2 reduction in pure water based on undoped and Co-doped $CsPbBr_3/Cs_4PbBr_6$ with various doping concentrations.[55] (c) Comparison chart of the yields between Mn-doped optimum catalyst sample 2 and $CsPbBr_3$.[106]

Inspired by it, some scholars have proven the theory. Dong *et al.* promoted the catalytic activity of perovskite NCs in visible light-driven CO_2 reduction by increasing the number of catalytic sites and improving charge separation through direct doping of Co cations on the $CsPbBr_3/Cs_4PbBr_6$ surface.[55] $Co_{1\%}$@NCs doped with Co achieve higher CO yields (1385 mmol g^{-1}) compared to the undoped NCs (678 mmol g^{-1}) in a 15 h reaction (Fig. 10b). In addition, Mn doping is also an effective strategy. Liu's group demonstrated a Mn-doped $CsPb(Br/Cl)_3$ mixed halide perovskite as a catalyst to improve CO_2 photoreduction efficiency.[106] A series of $CsPb(Br/Cl)_3$:Mn perovskites were obtained by adjusting the Mn content. For the optimum catalyst sample, the yield of CO reached 1917 μmol g^{-1} which is 14.2-fold higher than that of $CsPbBr_3$ (Fig. 10c).

3.3.4 Crystal plane regulation. Crystal faces of LHPs also play a pivotal role in determining their catalytic activity and selectivity for CO_2 reduction. Shyamal *et al.* prepared $CsPbBr_3$ materials with different exposure surfaces for photocatalytic CO_2 reduction.[107] Polyhedral non-cubic, hexapod and cubic $CsPbBr_3$ nanocrystals were synthesized, which are schematically shown in Fig. 11a. Despite having similar surface areas, the halogen deficient polyhedral $CsPbBr_3$ exhibits superior CO_2 reduction activity compared to the halogen-rich cubic $CsPbBr_3$. DFT calculations indicate that the reactivity is facet-dependent with the activity order of (112) > (102) > (002) > (110). Thus, polyhedral $CsPbBr_3$ with the (112) facet would be a more efficient photocatalyst for CO_2 reduction compared to hexapod and cubic $CsPbBr_3$ (Fig. 11b).

3.3.5 Encapsulation. Encapsulation has been demonstrated to be an effective method to prevent the decomposition of halide perovskites and improve their stability. Chen *et al.* synthesized microporous crystals of BIF-122-Co and encapsulated $CsPbBr_3$ perovskites as the main substrate to obtain a composite $CsPbBr_3$/BIF-122-Co (Fig. 12a) with high

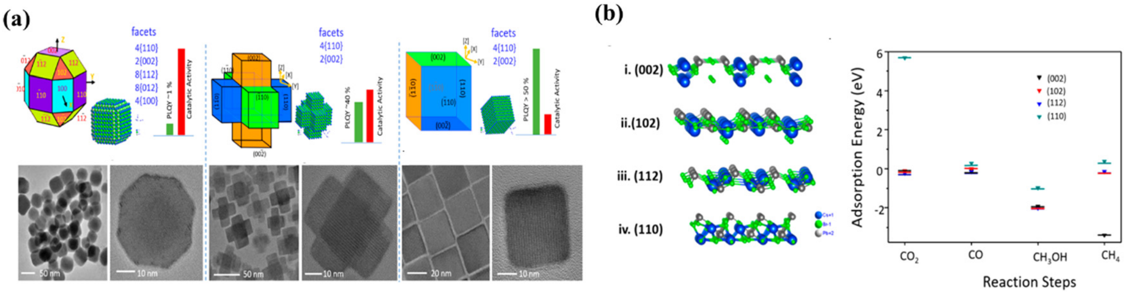

Fig. 11 (a) Models showing polyhedral noncube-, hexapod-, and cube-shaped $CsPbBr_3$ nanostructures, respectively. In each case, facets were labeled according to the assigned viewing axis and are also listed separately. Approximate PLQYs and observed catalytic activity in CO_2 reduction are provided in bar diagrams. TEM and HRTEM images of noncube-, hexapod-, and cube-shaped nanostructures, respectively.[107] (b) Atomic model showing the (002), (102), (112) and (110) facets of orthorhombic $CsPbBr_3$ (*Pbnm*) and adsorption energies of CO_2, CO, CH_3OH, and CH_4 on top of (002) (black), (102) (red), (112) (blue), and (110) (cyan) facets.[107]

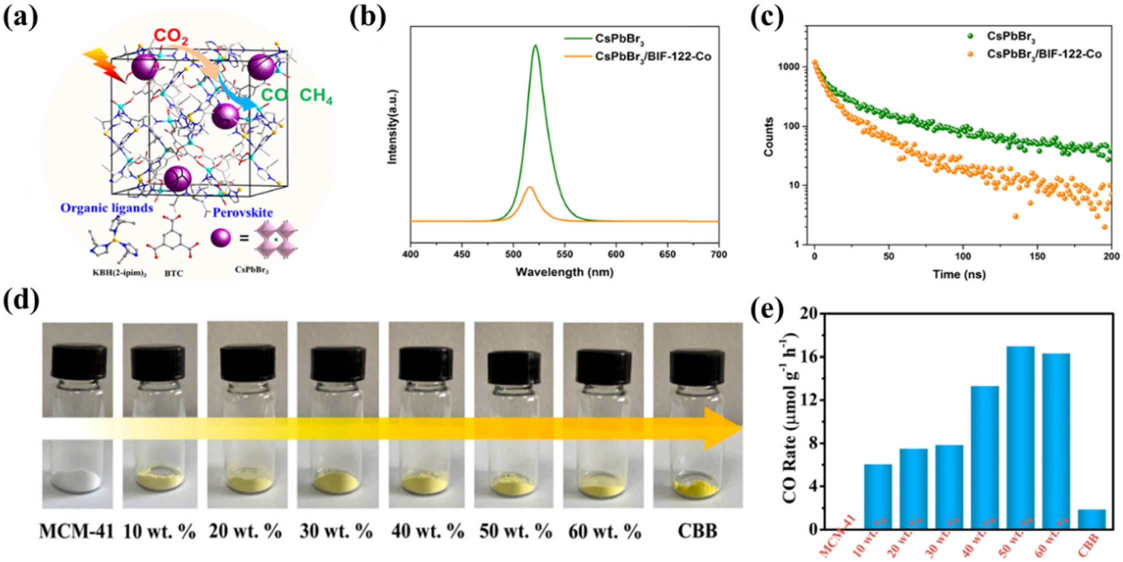

Fig. 12 (a) Schematic illustration of the surface modification of $CsPbBr_3$ NCs.[108] (b) Schematic representation of CO_2 photoreduction over the $CsPbBr_3$–Ni(tpy) photocatalyst system.[108] (c) The $CsPbBr_3$ QDs were anchored on the polymeric semiconductor g-C_3N_4 porous nanosheets *via* strong N–Br bonds.[108] (d) The MCM-41, CBB and MCM-41 supported CBB with different weight ratios.[109] (e) The photocatalytic performance of CBB, MCM-41 and CBB loaded in MCM-41 with different weight ratios.[109]

photocatalytic CO_2 reduction activity.[108] PL spectroscopy and electrochemical experiments indicate (Fig. 12b and c) that photogenerated electrons in the encapsulated $CsPbBr_3$ could be rapidly transferred to BIF-122-Co, thereby inhibiting electron–hole complexation in individual $CsPbBr_3$. Moreover, the porous BIF-122-Co backbone in the composite also significantly improves the stability of $CsPbBr_3$ perovskites in the photocatalytic reaction system. Mesoporous molecular sieves have received great attention as adsorbents, catalysts, and catalyst supports. Cui *et al.* synthesized space-restricted lead-free halide perovskite $Cs_3Bi_2Br_9$ in MCM-41 molecular sieve using a simple and effective impregnation method (Fig. 12d).[109] The MCM-41@CBB ($Cs_3Bi_2Br_9$) composite material shows excellent performance in photocatalytic reduction of CO_2 to CO under visible light irradiation and gas–solid conditions, in which CO generation rate of MCM-41@50 wt% CBB was measured to be 17.24 μmol g^{-1} h^{-1}, far exceeding that of pure CBB (1.89 μmol g^{-1} h^{-1}) (Fig. 12e). Similarly, very recently, Zhang's team have grown $Cs_2AgBiBr_6$ (CABB) nanocrystals *in situ* in MCM-48 mesoporous molecular sieve for photocatalytic CO_2 reduction.[110] The CABB@MCM-48 composite material shows excellent performance, far surpassing that of the original CABB. Such excellent photocatalytic performance of CABB@MCM-48 is attributed to enhanced CO_2 adsorption, effective charge separation and an abundance of active sites.

3.3.6 Surface finishing. Surface properties of semiconductors play a critical role in facilitating reactant adsorption, product desorption, and interfacial charge transfer. Therefore, the development of an effective surface modification strategy for halide perovskites is fundamental to achieving optimal

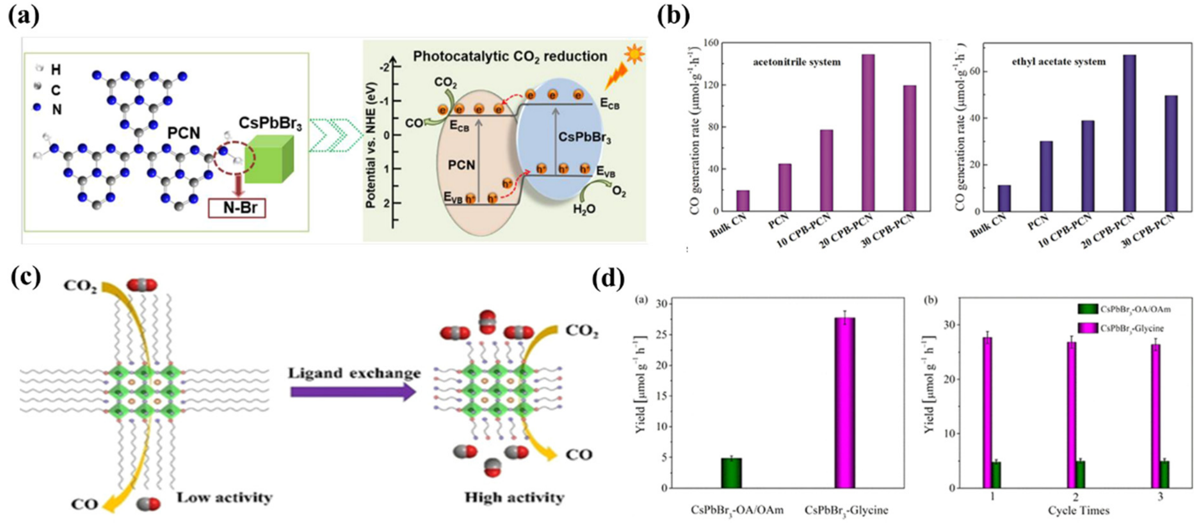

Fig. 13 (a) CsPbBr$_3$ QDs were anchored on the polymeric semiconductor g-C$_3$N$_4$ porous nanosheets *via* strong N–Br bonds.[111] (b) Generation of CO in the acetonitrile/water (left) and ethyl acetate/water system (right) over various photocatalysts.[111] (c) Glycine-functionalized CsPbBr$_3$ nanocrystals are constructed through a facile ligand-exchange strategy.[112] (d) Yields of CO generated from CO$_2$ reduction with CsPbBr$_3$-OA/OAm and CsPbBr$_3$–glycine NCs as photocatalysts, under Xe-lamp irradiation for 4 h with a 400 nm filter and a light intensity of 100 mW cm^{-2} (left) and yields of CO generated from CO$_2$ reduction for three consecutive cycles of 4 h each with CsPbBr$_3$-OA/OAm and CsPbBr$_3$–glycine NCs as photocatalysts (right).[112]

photocatalytic performance. The strategy is especially crucial given that the performance of these materials is highly dependent on their surface properties. Fig. 13a shows a composite photocatalyst system constructed by Xu *et al.* using N–Br chemical bonding to immobilize CsPbBr$_3$ quantum dots on the surface of NH$_x$-rich porous g-C$_3$N$_4$ nanosheets.[111] This composite photocatalyst exhibits good stability and high yield of 149 μmol h^{-1}g^{-1} in the acetonitrile/water system, which is 15-fold higher than that of the pristine CsPbBr$_3$ quantum dots. The special N–Br bonding state led to enhanced charge separation between the two materials and improved charge carrier lifetime, contributing to excellent photocatalytic performance (Fig. 13b). Besides, ligand capping is essential for the preparation of stable MHP nanocrystals (NCs). For example, Xu *et al.* constructed CsPbBr$_3$ nanocrystals with short-chain glycine as a ligand through a ligand exchange strategy.[112] Photogenerated carrier separation and CO$_2$ absorption are significantly improved due to the reduced site barrier of glycine and the presence of amine groups in the glycine without affecting the stability of the MHP NCs (Fig. 13c). The yield of CsPbBr$_3$ nanocrystals with glycine ligands for photocatalytic CO$_2$ conversion to CO without any organic sacrificial reagent increased significantly to ~27.7 μmol g^{-1} h^{-1} (Fig. 13d), which is 5-fold higher than that of CsPbBr$_3$ NCs with conventional long alkyl capped ligands (OA-OAm).

3.3.7 Heterogeneous junction engineering. The construction of heterogeneous structures is generally considered to be an effective method that can overcome the limitations of single catalysts, namely slow electron transfer and severe radiation compounding. Heterojunctions improve the photocatalytic efficiency by optimizing the electron 'path' and transferring electrons and holes to minimize the loss rate of valuable electrons–holes. Specifically, by choosing two (or more) semiconductor materials, heterojunctions are formed by suitable synthesis methods. A matched energy band arrangement can significantly accelerate carrier transfer and suppress recombination. It is generally accepted that there are three types of heterogeneous junction structures: type I (spanning gap) (Fig. 14a),

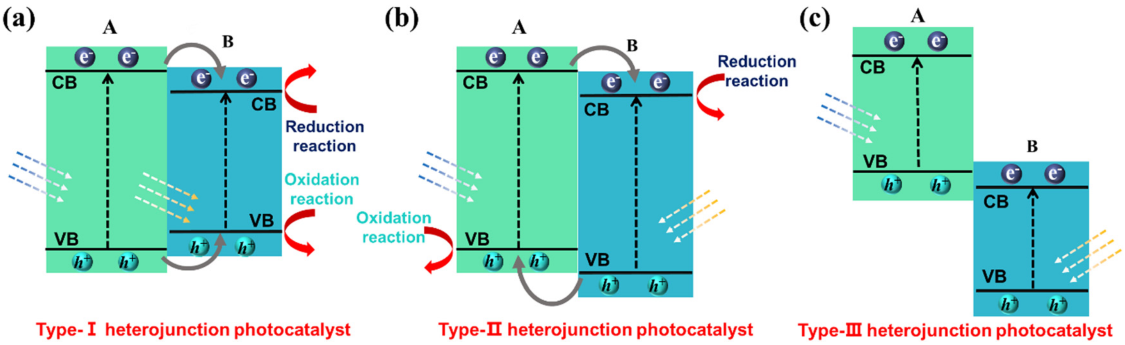

Fig. 14 Schematic illustration of electron–hole separation of three conventional heterojunctions: (a) type-I, (b) type-II and (c) type-III.

type II (staggered gap) (Fig. 14b) and type III (fractured gap) (Fig. 14c). Of these, type II heterojunctions are considered as the most suitable for facilitating the separation of photogenerated carriers due to the spatial separation of photogenerated electrons and holes that are transferred to different semiconductors.

3.3.7.1 Type-II heterojunction photocatalysts. Type-II heterojunctions offer a promising avenue for enhancing photocatalytic activity by promoting efficient separation of carriers. The well-matched band structure in these heterojunctions facilitates the transfer of charge carriers from one material to another, reducing the likelihood of recombination and enabling more effective use of light energy. Based on the above considerations, a large number of related studies have been conducted. For example, Wang *et al.* reported for the first time the *in situ* construction of a Cs_2SnI_6/SnS_2 heterostructure with a conventional type II band alignment structure for CO_2 photoreduction (Fig. 15a).[113] Li *et al.* developed a type-II ZnSe–$CsSnCl_3$ heterojunction composite (Fig. 15b), which exhibits enhanced photocatalytic activity.[114] Experimental results demonstrate that the ZnSe–$CsSnCl_3$ heterojunction structure could inhibit charge carrier irradiation and drive the transport of photogenerated electrons and holes in opposite directions. More importantly, $CsSnCl_3$ perovskites enable the ZnSe–$CsSnCl_3$ heterojunction composites to possess higher catalytic activity and lower their CO_2 reduction free energy. Besides, Wang *et al.* designed and synthesized $CsPbBr_3$/UiO-66(NH_2) nano-heterojunction composites (Fig. 15c), enabling conversion of CO_2 to fossil fuels in non-aqueous media with a significant increase in photocatalytic CO_2 reduction activity.[115] Fig. 15d shows an increasing trend in CO yield of the composite samples throughout the photocatalytic process. The significantly enhanced photocatalytic activity can be attributed to the rapid charge separation and transfer at the interface between $CsPbBr_3$ QDs and UiO-66(NH_2) nanocomposites. In addition, the large accessible specific surface area and enhanced visible light absorption are also responsible for the high activity of $CsPbBr_3$ QDs and UiO-66(NH_2) nanocomposites.

When considering the thermodynamics of a type-II heterojunction, the junction can exhibit exceptional electron–hole separation efficiency. This phenomenon can be attributed to the fact that the electrons are transferred to the conduction band with a weak reduction potential for reaction, while the holes are transferred to the valence band with a weak oxidation potential (as illustrated in Fig. 16a). From the kinetics perspective, it is important to note that the existence of original photogenerated electrons in semiconductor B can actually inhibit the continuous transfer of electrons from semiconductor A. Similarly, the presence of photogenerated holes in semiconductor A can hinder the transfer of holes from semiconductor B. This limitation ultimately restricts the improvement of carrier separation efficiency in a type-II heterojunction. Although the thermodynamic properties of type-II heterojunctions can facilitate enhanced charge separation, the kinetic limitations should be carefully considered to maximize their full potential.

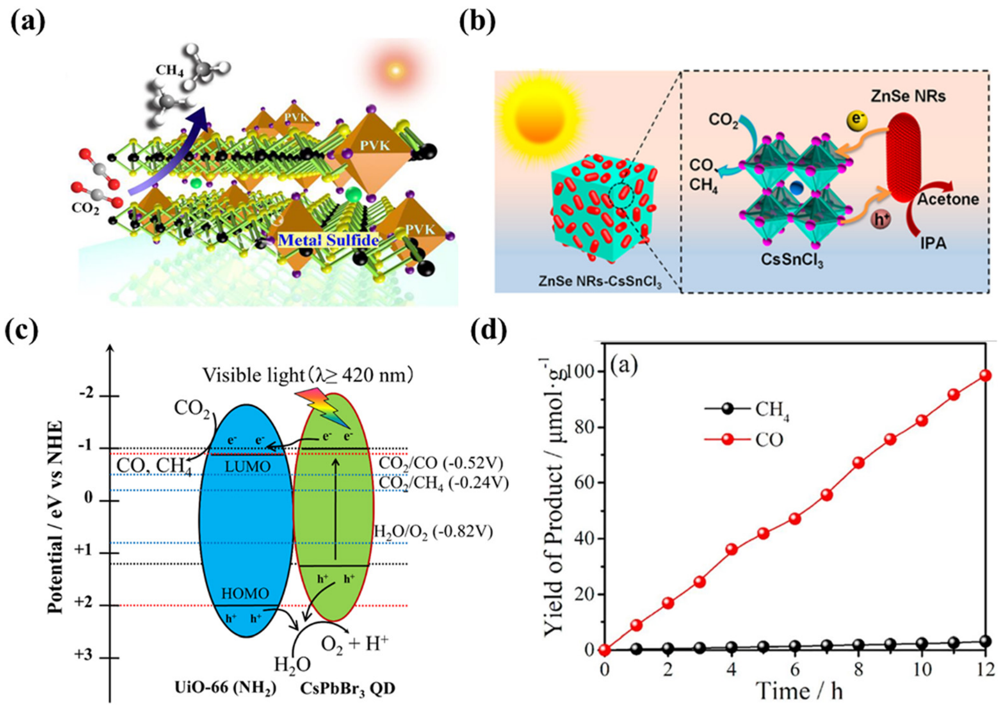

Fig. 15 (a) Schematic illustration of the photocatalytic CO_2 reduction.[113] (b) Schematic representation of the CO_2 photoreduction process on ZnSe–$CsSnCl_3$.[114] (c) Schematic illustration of the possible mechanism of photocatalytic CO_2 reduction on $CsPbBr_3$/UiO-66(NH_2).[115] (d) Photocatalytic CO_2 reduction into chemical fuels under a 300 W Xe lamp for 15%-$CsPbBr_3$ QDs/UiO-66(NH_2).[115]

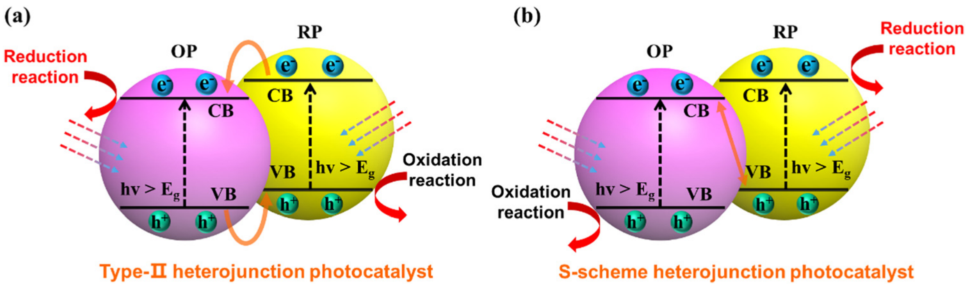

Fig. 16 Schematic illustration of electron–hole separation of a (a) conventional type-II heterojunction photocatalyst and (b) S-scheme heterojunction photocatalyst.

3.3.7.2 Direct-Z (S) heterojunction photocatalysts. The concept of the Z-type heterojunction photocatalyst was first introduced by Bard in 1979,[116] and the name was given due to the electron transfer path bearing a resemblance to the letter 'Z' (as illustrated in Fig. 16b). It was not until 2013, however, that Yu *et al.* developed the first direct Z-type heterojunction photocatalyst (Fig. 17a), *i.e.*, g-C_3N_4/TiO_2.[117] The reduction and oxidation reactions of direct Z-type photocatalysts occur in semiconductors with more negative reduction potentials (RP) and more positive oxidation potentials (OP) respectively, resulting in stronger redox capabilities compared to type-II heterojunctions. In addition, Z-type heterojunctions allow for the separation of photogenerated carriers by direct transfer of electrons through interfacial transport and by means of redox in the intermediate medium, leading to a highly effective separation of photogenerated carriers. This exceptional carrier separation efficiency is one of the key features that sets Z-type heterojunctions apart from other types of heterojunctions, and has played a significant role in promoting the photocatalytic CO_2 reduction activity of MHP-based materials. Overall, the development of direct Z-type heterojunction photocatalysts has opened up a promising new avenue for advancing photocatalysis, and continued research in this area is expected to generate exciting new breakthroughs in the future.

Not long ago, the concept of direct Z-type heterojunctions was also successfully applied to MHP-based CO_2PR. For example, Yu *et al.* synthesized TiO_2/$CsPbBr_3$ heterojunction structures with S-type (direct Z-type) electron transfer pathways by a simple electrostatic self-assembly method, and the unique electron transfer pattern allows for a high spatial separation of electron–hole pairs to facilitate efficient CO_2 photoreduction (Fig. 17b).[118] More efficient charge separation between TiO_2 and $CsPbBr_3$ and enhanced photoreduction activity towards CO_2 due to IEF induction were demonstrated. DFT calculations show that the work function of TiO_2 is greater than that of $CsPbBr_3$, implying that electrons are transferred from $CsPbBr_3$ to TiO_2 during hybridization, resulting in an IEF at the interface. *In situ* XPS analysis demonstrates that the IEF drives the photoinduced electrons in the CB of TiO_2 to move into the VB of $CsPbBr_3$, confirming the S pathway of charge transfer. Bi_2WO_6 is widely used as a typical semiconductor photocatalyst for wastewater treatment, air purification and CO_2 reduction.[119,120] Recently, Bi_2WO_6 has also been explored for the construction of two-component heterojunction

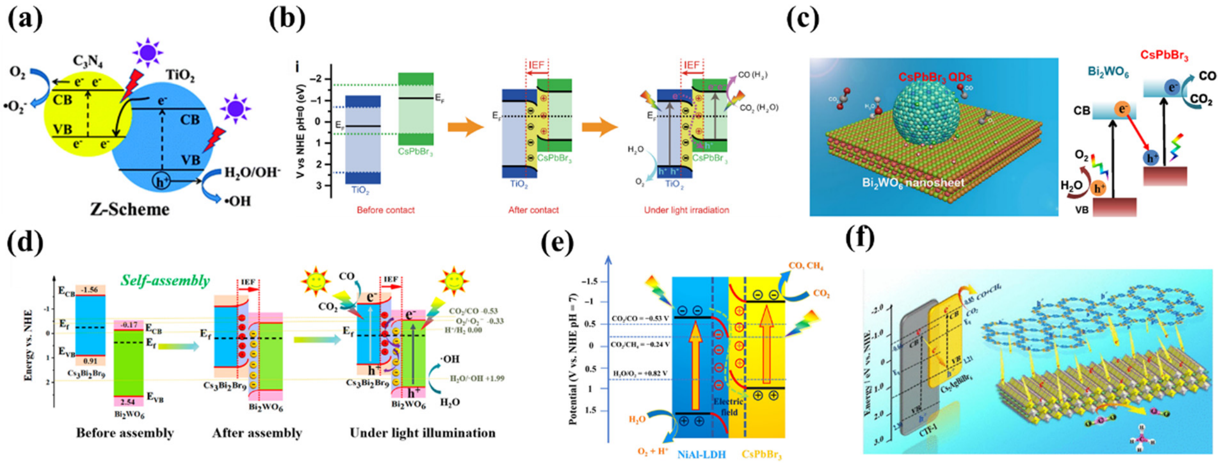

Fig. 17 (a) Diagram of a Z-shaped heterogeneous junction.[117] (b) Schematic illustration of the TiO_2/$CsPbBr_3$ heterojunction: internal electric field (IEF) induced charge transfer, separation, and the formation of an S-scheme heterojunction under UV visible-light irradiation for CO_2 photoreduction.[118] (c) 0D/2D CPB/BWO of the Z-scheme photocatalytic system for CO_2 reduction.[121] (d) Energy band bending and IEF formation for CBB and BWO assembly before and after, which strongly promotes the S-scheme photoelectron transfer during the CRR process.[122] (e) Proposed pathway for photocatalytic CO_2 reduction under visible light irradiation of $CsPbBr_3$/NiAl-LDH.[125] (f) Diagram of $Cs_2AgBiBr_6$/CTF-1 photoreduction.[127]

materials for efficient CO_2 photoreduction. For example, Wang *et al.* constructed a direct Z-type heterojunction by decorating 0D $CsPbBr_3$ onto 2D Bi_2WO_6 nanosheets (Fig. 17c).[121] The close contact between 0D $CsPbBr_3$ and 2D Bi_2WO_6 nanosheets facilitates charge separation and transfer between the two semiconductors. Similarly, Feng's group fabricated $Cs_3Bi_2Br_9$/Bi_2WO_6 (CBB/BWO) S-type heterojunctions with 0D/2D structures by adopting an electrostatic self-assembly method.[122] The composite achieves a CO generation rate of 220.1 μmol g^{-1} h^{-1}, which is 115.8 and 18.5 times higher than that of CBB PQDS and BWO NS, respectively. High performance is mainly attributed to the close heterogeneous surface contact between CBB PQDS and BWO NS, which facilitates effective space charge separation and shortens the charge transfer distance (photoelectron transfer process before and after the S-type heterojunction assembly is shown in Fig. 17d). Layered double hydroxides (LDHs), as a class of two-dimensional layered materials, have been widely used in photocatalysis due to their unique layered structure, environmental friendliness, tunable electronic band structure, flexible chemical composition and strong CO_2 adsorption capacity.[123,124] For instance, Zhao *et al.* reported that $CsPbBr_3$ nanocrystals are activated by the layered double hydroxide nanosheets (CLDH) to boost the photocatalytic CO_2 reduction (Fig. 17e).[125] These CLDH without any co-catalysts and sacrificial agents show significantly enhanced CO_2 photoreduction performance and the average electron consumption rate of CLDH (49.16 μ^{-1} h^{-1}) is approximately 3.7 times higher than that of pure $CsPbBr_3$. Covalent organic frameworks (COFs) are a family of highly crystalline organic semiconductors that have potential applications in a variety of fields due to their large surface area and abundant pores. As a branch of COFs, two-dimensional covalent triazine frameworks (CTFs) are very attractive because their rich triazine units have given them some special advantages, namely excellent chemical and thermal stability, high carrier mobility, and powerful CO_2 adsorption and activation capabilities.[126] $Cs_2AgBiBr_6$/CTF-1 (CABB/CTF-1) composites were designed by Zhang *et al.* through a self-assembly method (Fig. 7f), where the large surface-to-surface contact area of the 2D structure ensures intimate interfacial interactions and effective charge transfer/separation.[127] Meanwhile, the periodic pore structure of CTF-1 enables the CABB/CTF-1 composite photocatalyst to provide stronger CO_2 adsorption/activation capability.

In general, type-II and direct Z-scheme heterojunctions have emerged as two promising approaches for promoting the photocatalytic activity by enhancing the spatial separation of charge carriers. While direct Z-scheme heterojunctions have been shown to exhibit even higher separation efficiency of electrons and holes compared to type-II heterojunctions, there is still much place to be explored in terms of constructing MHP-based Z-scheme heterojunctions and characterizing the electron transfer pathways involved. Further research is necessary to fully understand the mechanisms in the heterojunctions and optimize their performance for practical applications.

4. CO_2 photoreduction products beyond CO

Equations for the redox reactions of possible products in the photocatalytic CO_2 reduction process are listed in Table 1, which can provide useful insights into the equilibrium potential and reaction enthalpy. To date, most perovskite-based photocatalysts facilitate a two-electron reduction process to CO. Selective photocatalytic reduction of CO_2 to CH_4 is much more difficult to accomplish as it is an eight-electron process, but the production of CH_4 is also very important in terms of the energy source.[128] It is a major component of natural gas and is widely used for electricity generation, heating and fuel transportation.[129] Furthermore, CH_4 is a raw material for many important chemical compounds such as CH_3OH, C_2H_4 and C_3H_6. These compounds are used extensively in the

Table 4 MHP-based catalysts for CO_2PR with CH_4-dominated products

Photocatalyst	Light source	System	$R_{\text{total electron}}$ (μmol g^{-1} h^{-1})	Products	Selectivity (%)	Ref.
Fe:$CsPbBr_3$	450 W Xe-lamp	EA/H_2O	55	CH_4, CO	∼100	55
$CsPbBr_3$/BIF-122-Co	—	EA/H_2O	90.67	CH_4, CO, H_2	57.5	108
Cs_2SnI_6/SnS_2	100 W Xe lamp, $\lambda > 400$ nm	CH_3OH/H_2O	16	CH_4	∼100	113
$CsPbBr_3$@g-C_3N_4	—	EA	59.98	CH_4, CO	∼100	117
Pt–$CsPbBr_3$/Bi_2WO_6	150 W Xe lamp, AM 1.5G	EA/IPA	324.0	CH_4, CO, H_2	95.4	119
$Cs_3Bi_2Br_9$@M-Ti	720 nm $\geq \lambda \geq$ 420 nm	IPA	202.68	CH_4, CO	∼100	130
$Cs_2AgBiBr_6$@M-Ti	720 nm $\geq \lambda \geq$ 420 nm	IPA	271.58	CH_4, CO	∼100	130
Cd:$CsPbBr_3$	450 W Xe-lamp	EA/H_2O	338.4	CH_4, CO	∼100	131
Ti_3C_2/$CsPbBr_3$ QDs	300 W Xe-lamp	EA	190.44	CH_4, CO	∼100	135
Cu scaffold with $CsPbBr_3$ film	—	EA/H_2O	251.88	CH_4, C_2H_4, C_2H_6, C_3H_8, H_2	93.27	141
$CsCuCl_3$ MCs	AM 1.5G 100 mW cm^{-2}	EA/IPA	32.66	CH_4, CO	∼100	197
$CsPbBr_3$ (Cd ∼3%) star	450 W Xe lamp, $\lambda > 420$ nm	EA/H_2O	237.2	CH_4, CO	∼100	210
$CsPbBr_3$ NC/a-TiO_2	150 W Xe-lamp, AM 1.5G	EA/IPA	64.45	CH_4, CO, H_2	95.5	211
$CsPbBr_3$@ZIF-8	100 W Xe lamp, AM 1.5G	H_2O (vapor)	15.498	CH_4, CO	∼100	212
$CsPbBr_3$@ZIF-67	100 W Xe lamp, AM 1.5G	H_2O (vapor)	29.630	CH_4, CO	∼100	212
$CsPbBr_3$/GO	500 W Xe-lamp, $\lambda > 400$ nm	H_2O (vapor)	162.6	CH_4, H_2	91.5	213
$CsPbBr_3$ NC/BZNW/MRGO	$\lambda > 420$ nm, AM 1.5G	H_2O (vapor)	52.02	CH_4, CO	∼100	214
α-Fe_2O_3/amine-RGO/$CsPbBr_3$	150 W Xe lamp, $\lambda > 420$ nm	H_2O (vapor)	80.95	CH_4, CO, H_2	99.3	215
$CsPbBr_3$ NS–Cu–RGO	—	H_2O (vapor)	∼103	CH_4, CO, H_2	∼99.4	216

manufacture of plastics, fertilizers, solvents and other chemical products. Therefore, the exploration of efficient photocatalysts for the conversion of CO_2 to CH_4 is of great significance in both energy and chemical industries. Table 4 summarizes the recent studies on MHP-based CO_2PR with CH_4-dominated products. Mesoporous materials are a class of star materials with an open pore structure and a large specific surface area, making them ideal for catalytic reactions. Meanwhile, rational design of the structure of the mesoporous shell could facilitate the accelerated separation of electron–hole pairs. Recently, Sun *et al.* reported the synthesis of CBB@M-Ti and CABB@M-Ti by growing lead-free perovskite nanodots $Cs_3Bi_2Br_9$ (CBB) and $Cs_2AgBiBr_6$ (CABB) in mesoporous titanium dioxide (M-Ti) frameworks for photocatalytic CO_2 reduction (Fig. 18a).[130] M-Ti and the formation of an IEF between the CBB and CABB interfaces induce the electron–hole separation. CBB@M-Ti and CABB@M-Ti show high CH_4 yields of 151.1 and 144 μmol g^{-1} with a selectivity of 88.7% and 84.2%, which are significantly higher than those of M-Ti, CBB and CABB. DFT calculations suggest that the high selectivity of CH_4 can be attributed to double adsorption-mediated hydrogenation of CO to *HCO rather than CO desorption (Fig. 18b). A special phase structure of perovskite can also increase the selectivity of the CH_4 product. For instance, Bera's group synthesized helical $CsPbBr_3$ nanorods using a prelattice of orthorhombic phase Cs_2CdBr_4 with Pb(ɪɪ) diffusion, where helicity is achieved by controlling the composition of the alkylammonium ions in the reaction system and selectively dissolving some of the helical facets of the nanorods (Fig. 18c).[131] The optimum catalyst (<3% Cd) achieves the yields of 40.81 μmol g^{-1} h^{-1} (CO) and 74.45 μmol g^{-1} h^{-1} (CH_4) and CH_4 selectivity as high as 87.9% (Fig. 18d). Despite these efforts on the photoconversion of CO_2 to CH_4 based on MHPs, higher selectivity and yield of CH_4 are still required, which needs further in-depth understanding of the reaction mechanism, optimization of catalyst design and tuning of reaction conditions and surface properties.

In addition to the two main products (*i.e.*, CO and CH_4), the photoreduction of CO_2 to multi-carbon products appears to be more attractive and challenging. The reason is that multi-carbon products usually have a higher economic value and energy density.[132] Meanwhile, compared to CO and CH_4, multi-carbon compounds possess wider potential for application in the chemical, energy and material sectors.[133] Despite the diversity of catalytic systems observed for C_{2+} products, there are hardly any experimental reports on the production of C_{2+} products with MHP-based photocatalytic systems.[134–136] The difficulty of MHPs for the production of C_{2+} may be understood in that the general process of e^-/h^+ recombination limits the transfer of multiple electrons in a short period of time, thus leading to an energy waste that not only decreases CO_2 conversion but also results in product selectivity towards C_1.[137] It has been found that the multiple electrons coupled to proton transfer (MECPT) reactions, along with C–C coupling steps, play a crucial role in the formation of C_{2+} products.[138] In recent years, Cu-based catalysts have been extensively reported for the preparation of multi-carbon products by (photo)electrochemical CO_2 reduction.[139,140] Therefore, the utilization of Cu-based catalysts to tune the reaction selectivity toward C_{2+} products may be an effective choice. Recently, as a pioneering study, Choi's group reported for the first time the use of MHP-based catalysts for the generation of multi-carbon products.[141] They prepared a composite photocatalyst by embedding $CsPbBr_3$ nanocrystals in a porous Cu scaffold and applied this integrated catalyst for photocatalytic CO_2 reduction reaction (Fig. 19a). As a result, ethylene (C_2H_4, 46.5 μmol g^{-1}) is detected as the main product, together with the formation of methane (CH_4, 18.9 μmol g^{-1}), ethane (C_2H_6, 17.1 μmol g^{-1}) and propane (C_3H_8, 11.3 μmol g^{-1}) (Fig. 19b). The reason behind the generation of multi-carbon products can be associated with

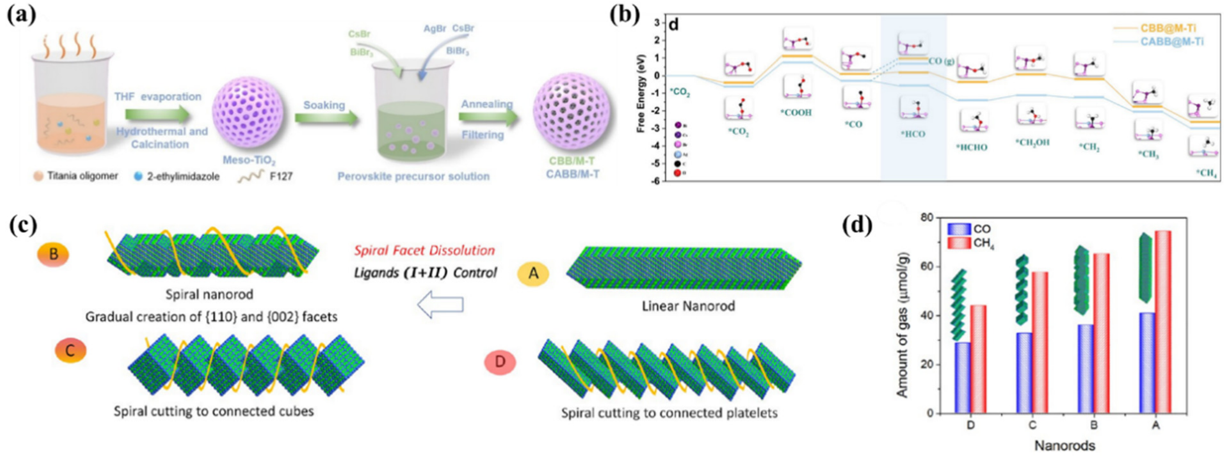

Fig. 18 (a) Schematic illustration of the synthesis of *X*% CBB@M-Ti and CABB@M-Ti.[130] (b) Gibbs free energy pathway for the formation of CH_4 and CO from CO_2 over CBB@M-Ti and CABB@M-Ti.[130] (c) Models showing $CsPbBr_3$ nanorods spirally cutting to different spiral nanorods with different reaction conditions of A to D. For the case of C, models are done with normal cubes though truncated shaped were observed. All these models are schematic and were designed using Diamond Crystal Impact software. Cs atoms in all cases were kept on surfaces.[130] (d) Comparison of photocatalytic CO_2 reduction activity of four $CsPbBr_3$ nanorods.[131]

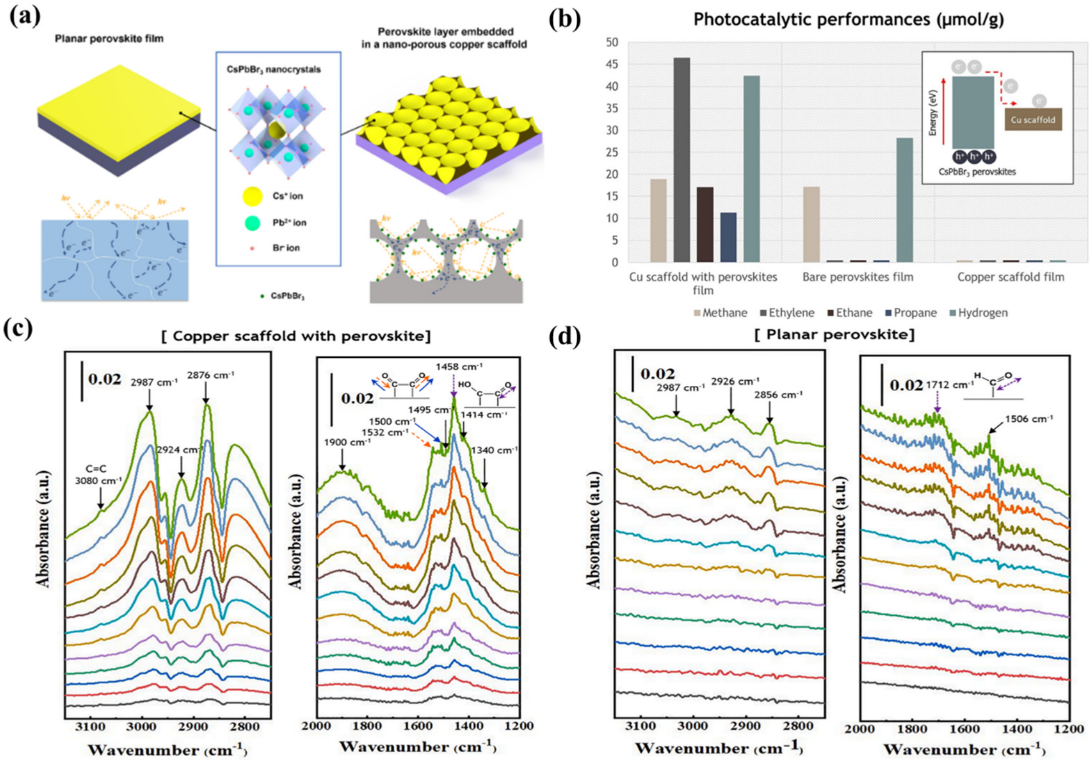

Fig. 19 (a) Comparison of the charge transport processes in a planar perovskite film and the perovskite layer embedded in a nanoporous copper scaffold.[141] (b) Yield of the CO_2 reduction products after 5 h of photochemical reaction. The inset image represents the relative energetic diagram of the $CsPbBr_3$ perovskites within a porous copper scaffold, which acts as an assistant for electron transfer in photocatalytic CO_2 reduction.[141] (c) *In situ* ATR-IR spectra of photocatalytic CO_2 reduction on the $CsPbBr_3$ perovskite photocatalyst embedded in a porous copper scaffold.[141] (d) *In situ* ATR-IR spectra of photocatalytic CO_2 reduction on the $CsPbBr_3$ perovskite photocatalyst embedded in a porous copper scaffold.[141]

the copper support and the graded porous structure. For an in-depth understanding of the photocatalytic CO_2 reduction mechanism, *in situ* ATR-IR measurements were carried out (Fig. 19c and d). The results show that the C_1 reaction pathway leading to CH_4 dominates on the bare planar perovskite, while the C_2 reaction pathway leading to C_2H_4, C_2H_6 and C_3H_8 is evident on the perovskite embedded in a porous Cu support. *CHO triggers the C_1 pathway of CO_2 reduction on the bare planar perovskite, leading to the formation of CH_4. In contrast, *OCCO generated *via* CO dimerization on the perovskite embedded in porous Cu stents triggers the C_2 pathway. It is believed that this pioneering work will provide inspiration for the subsequent development of highly efficient MHP-based CO_2PR for multi-carbon products.

5. Conclusion and outlook

In this review, we present a timely and comprehensive review of recent advances in MHP-based CO_2PR. Firstly, the review describes the structure and photoelectric properties of MHPs. Then, various strategies are summarized for improving the efficiency of CO_2PR to CO, using lead-based and lead-free MHP materials. Moreover, detailed discussions are given about the MHP-based CO_2PR to CH_4 and C_{2+} products, with a focus on the design strategies for enhancing specific selectivity.

Although remarkable advances in this field have been made, several challenges still exist. In our opinion, future research efforts for MHP-based CO_2 photoreduction should focus on the following aspects, as schematically shown in Fig. 20.

5.1 Exploiting new MHPs

5.1.1 Stable MHPs. The physical and chemical instability of MHPs under high temperature, humidity or an oxidizing atmosphere could significantly reduce their operational lifetime, which prompts researchers to seek effective solutions to improve the stability of MHPs. Some studies have shown that partial or total replacement of Pb in MHPs with other metallic elements (*e.g.*, Cu, Bi) has proven to be an effective strategy for improving the stability of MHPs.[142,143] In addition, optimizing the crystal growth conditions, such as temperature and humidity, can help to minimize the presence of defects and impurities that may lead to degradation of the crystal structure. Moreover, special encapsulation materials (*e.g.*, polymer films) or inorganic coatings (*e.g.*, SiO_2, TiO_2, C_{60}, r-GO and g-C_3N_4) can be utilized to shield MHPs from the external environment and enhance their stability.[144,145] Specifically, the surface encapsulation prevents MHPs from coming into direct contact with the external environment and acts as a solid barrier to water and other polar solvents. Physical confinement also inhibits anion exchange and ion migration at the MHP surface. Replacing the

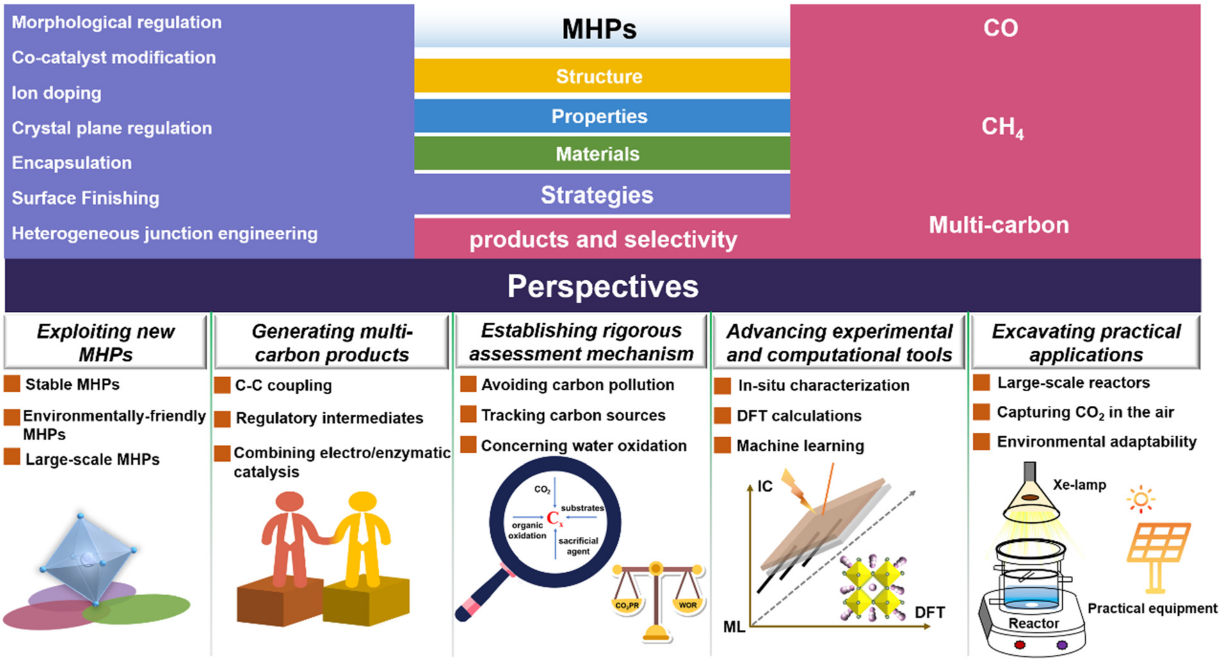

Fig. 20 Future research perspectives of MHPs for photocatalytic CO_2 reduction.

long chain OA/OAm with other suitable ligands could also passivate the surface of the perovskites and prevent degradation of the MHPs, preserving their structural stability for extended time periods.[112] These solutions will enable MHPs to maintain their photoelectric performance and stability, thereby extending their lifespan and improving their overall performance.

5.1.2 Environmentally friendly MHPs. Lead toxicity is a major challenge for the long-term viability of MHPs. To address this problem, there has been ongoing search for atoms with similar radii as potential replacement of lead in MHPs. Some of the promising alternatives are Ag, Sn, Rb, Bi, In and Ge. Of these alternatives, Bi-based perovskites have shown great potential for application in CO_2 photoreduction.[45,86] Continuous research efforts into these alternatives are essential for the development of sustainable MHPs. In addition, the manufacturing process of some MHPs may present extra environmental impacts, including the release of polluting gases. To alleviate these concerns, it is also important to optimize the production processes and reduce harmful emissions. These approaches will help pave the way for the future development of green MHP-based photoreduction, where MHPs are produced and utilized with minimal impact on the environment.

5.1.3 Large-scale MHPs. To date, most research studies on the photocatalytic reduction of CO_2 to solar fuels are limited to the laboratory scale. On the one hand, the recovery of catalysts is both expensive and time-consuming. On the other hand, the reaction kinetics of photocatalysis are sluggish and the product conversion rates are low. In order to achieve industrial-scale production of MHP-based photocatalysts, optimization of the synthetic protocols and material composition could be considered, leading to cost-efficiency and high photoconversion efficiency.

5.2 Generating multi-carbon products

So far, the MHP-based CO_2PR products are mainly C_1 products (*i.e.*, CO and CH_4), while C_{2+} products have rarely been reported. This can be explained by the severe radiative recombination of MHPs which limits the migration of multiple electrons in a short period of time, and the slow kinetics of the C–C coupling reaction which leads to high reaction energy barriers as well as low multi-carbon product selectivity.[146,147] In order to design efficient MHP-based photocatalysts and exert control over the reaction pathways for desired products, some suggestions are given: (1) exploring the potential of Cu-based photocatalysts for CO_2PR. Extensive research has demonstrated that the Cu-based materials are effective in promoting C–C coupling in CO_2 electroreduction for C_{2+} products, which could inspire the exploration of Cu-based photocatalysts for the generation of C_{2+} products. It is emphasized that the driving force behind C–C coupling does not stem from specific elements (*e.g.* Cu). Actually, the asymmetric charge distribution leads to the formation of high electron density centers which are needed for multi-electron requirements, ultimately driving the C–C coupling reactions.[147] Recent studies have also demonstrated that the excellent conversion of C_{2+} products by Cu-based catalysts depends largely on their good adsorption capacity for most of the C_{2+} intermediates.[148–150] This feature is conducive to causing charge polarization, which induces the C–C coupling reaction. In view of this, it is worthwhile to explore the development of composite catalysts by combining MHPs with Cu. Constructing photocatalytic systems with heterogeneous Cu species and further optimizing through charge polarization strategies may be conducive to achieving efficient CO_2PR for the production of C_{2+} chemicals. (2) Regulatory intermediates. It is widely accepted that CO is the key intermediate in the formation of multi-carbon products through the process of dimerization (in the form of CO–CO) or coupling (in the form of CO–COH) pathways.[151,152] Obviously, these steps necessitate the presence of the precursor, referred to as the steady-state adsorbed CO (*CO), in close proximity on the surface with a high coverage. Thus, enriching the *CO concentration and decorating active sites on MHPs can stabilize *CO. Subsequently, the adsorbed CO intermediates (*i.e.*, *CO) on adjacent sites create an asymmetric charge distribution, thereby enhancing the activation of CO and promoting the formation of key intermediates. (3) Combining electro/enzymatic catalysis. In recent years, photoelectrocatalysis and photoenzymecatalysis have shown great potential to convert CO_2 into multi-carbon products.[153–155] In a photocatalytic system, the internal charge separation and transfer processes occur within the absorbing nanoparticles, which are driven by the built-in electric field (IEF). However, these processes often encounter significant challenges, including severe charge recombination and insufficient driving force. To address these challenges, MHPs can be decorated as photocathodes to establish a photoelectrocatalysis system. By applying an external bias, charge separation can be effectively promoted. Additionally, the implementation of an ion membrane in the photoelectrocatalysis system spatially isolates the oxidation and reduction active sites, leading to the effective suppression of the reverse reaction. In addition to photoelectrocatalysis, another promising strategy is combining the biological-enzymes for CO_2PR. The biological-enzyme catalysts offer advantages such as high selectivity, environmental friendliness, mild operating conditions and facile carbon–carbon coupling, which facilitate the conversion of CO_2 into valuable products.[155] Recent studies have elucidated the participation of certain coenzymes in a multitude of vital metabolic reactions, where they play a facilitating role in the light-induced C–C coupling of short-chain carbon building blocks with long-chain carbons.[156,157] Hence, it is anticipated that the future integration of MHPs with specific enzymes to form photoenzymecatalysis systems will instigate research interest among scholars.

5.3 Establishing a rigorous assessment method

Some reports on MHPs have reported only a low conversion rate within the range of μmol g^{-1} in the experimental study of CO_2PR. In this case, very few detected products are most likely not from the photocatalytic CO_2 reduction. Therefore, several important factors need to be considered to demonstrate that the products are generated by the photocatalytic reduction of CO_2 and are not from accidental contamination or photooxidation of the organic system itself (*e.g.*, EA or ACN). (1) Avoiding carbon pollution. As most MHPs are water sensitive, the reaction system is mostly chosen to be carried out in an organic system (*e.g.* EA or ACN), which stabilizes the structure of the MHPs and promotes the solubility of CO_2. However, the organic system can bring some negative effect, such as unavoidable degradation of EA/ACN to CO/CH_4 in the presence of light and the oxidation of the sacrificial agent which may also give rise to the associated C_1 products.[158,159] To exclude the influence of solvents, it is advisable to utilize the ''solid–vapor reaction mode'' for water-sensitive systems.[160] Simultaneously, it is worth noting that certain preceding studies have demonstrated the enhanced photocatalytic performance through the integration of the MHP with a carbonaceous substrate. However, this approach neglects the adverse consequence whereby the photodegradation of carbonaceous catalysts may lead to the generation of a C_1 product.[85,191,193,198] To exclude possible contamination from the photodegradation of carbon substrates, it is critical to conduct control experiments utilizing pristine carbon substrates. Hence, to quantify the yield of photocatalysis in the presence of organic solvents or contaminants, it is necessary to carry out the reaction under inert conditions (N_2 or Ar) while keeping other conditions constant. Furthermore, control experiments under dark conditions using CO_2 to exclude the potential influence of chemical catalysis is equally important. To prove the effectiveness of photocatalytic CO_2 reduction convincingly, the product generation rate should significantly surpass that of control experiments. (2) Tracking carbon sources. Further definitive evidence that the detected products originate from the photoreduction of CO_2 requires isotopic labeling techniques using $^{13}CO_2$. Briefly, the accumulation of $^{13}C_x$ products should correspond to the amount of $^{12}C_x$ consumed in $^{12}CO_2$ under the same experimental conditions. (3) Concerning water oxidation. As mentioned above, a significant portion of the literature focuses on CO_2 reduction reactions employing sacrificial agents, which cannot be regarded as authentic artificial photosynthesis. Since many of the sacrificial agents are thermodynamically spontaneous, the introduction of a light source merely accelerates the progress of the reaction. Therefore, the crucial criterion for verifying the utilization of solar energy in achieving the conversion of CO_2 to chemical fuel is the occurrence of a water oxidation reaction (WOR). In other words, it is important to investigate whether simultaneous water oxidation takes place during the CO_2 reduction process. In short, establishing a rigorous measurement and evaluation method will make the results more persuasive.

5.4 Advancing experimental and computational tools

A precise understanding of the catalyst structure (*e.g.*, defects, atomic configurations and elemental arrangements) is beneficial to investigate the structure–activity correlation. To achieve this goal, a wide range of characterization techniques have been developed. Traditional *ex situ* characterization can only reflect the pre- and post-reaction state of a catalyst. For catalytic reactions, it is of great importance to probe the system under the real reaction conditions, such as real-time detection of the changes in the atomic structure of the catalyst, the intermediates of adsorbed molecules, the chemical state of the catalyst, and the displacement of ligand atoms. The state of the reaction intermediates is crucial to study the mechanism of the catalytic reaction. An accurate understanding of the catalyst structure can also help construct theoretical models that are more realistic, reasonable and valid. To unravel the above issues, employment of *in situ*/*operando* characterization techniques is necessary. Up to now, the real-time structures of MHPs during CO_2PR are seldom explored and in-depth investigation could shed more light on this aspect. Meanwhile, theoretical simulations (*e.g.*, machine learning and DFT calculations) have been regarded as a powerful tool to explain experimental results and predict catalytic performance, providing guidelines to speed up the development of new catalysts. Therefore, rigorous theoretical simulations in corroboration with advanced characterization techniques may be the best way to uncover the photocatalytic mechanism and explore high-efficiency photocatalytic systems.

5.5 Excavating practical applications

Conventional photocatalytic reactors are small devices and are mainly used for lab-scale proof-of-concept demonstrations. In order to achieve industrial-scale production, the development of large-scale flat-plate-reactors and reaction tanks can be considered. Besides, most of the photocatalytic conversions of CO_2 focus on high-purity CO_2 feed stream, requiring additional energy to capture and enrich CO_2. To address this issue, future technologies need to be designed to capture CO_2 directly in air and reduce it *in situ* to enable photoconversion at low CO_2 concentrations. Furthermore, photocatalysis also needs to consider the impact of the environment on the reaction. For example, light intensity, temperature, humidity and the presence of organic substances may potentially alter the reaction performances. Future research is required to provide more detailed understanding of the impact of these environmental factors on photocatalytic reactions and the adaptation of systems to different environmental conditions.

Conflicts of interest

The authors declare no competing financial interest.

Acknowledgements

This work was supported by the Natural Science Foundation for Young Scholars of Jiangsu Province (no. BK20220879), National Natural Science Foundation for Young Scholars of China (no. 22209072), and Jiangsu Specially-Appointed Professors.

References

1 L. Zhao, F. Ye, D. Wang, X. Cai, C. Meng, H. Xie, J. Zhang and S. Bai, *ChemSusChem*, 2018, **11**, 3524–3533.
2 J. K. Stolarczyk, S. Bhattacharyya, L. Polavarapu and J. Feldmann, *ACS Catal.*, 2018, **8**, 3602–3635.
3 J. Qiao, Y. Liu, F. Hong and J. Zhang, *Chem. Soc. Rev.*, 2014, **43**, 631–675.
4 T. Inoue, A. Fujishima, S. Konishi and K. Honda, *Nature*, 1979, **277**, 637–638.
5 F. Xu, K. Meng, B. Cheng, J. Yu and W. Ho, *ChemCatChem*, 2018, **11**, 465–472.
6 X. Zhang, X. Zhao, K. Chen, Y. Fan, S. Wei, W. Zhang, D. Han and L. Niu, *Nanoscale*, 2021, **13**, 2883–2890.
7 J. Wang, S. Lin, N. Tian, T. Ma, Y. Zhang and H. Huang, *Adv. Funct. Mater.*, 2020, **31**, 2008008.
8 M. Ou, W. Tu, S. Yin, W. Xing, S. Wu, H. Wang, S. Wan, Q. Zhong and R. Xu, *Angew. Chem., Int. Ed.*, 2018, **57**, 13570–13574.
9 C. Xie, W. Chen, S. Du, D. Yan, Y. Zhang, J. Chen, B. Liu and S. Wang, *Nano Energy*, 2020, **71**, 104653.
10 M. Baca, W. Kukulka, K. Cendrowski, E. Mijowska, R. J. Kalenczuk and B. Zielinska, *ChemSusChem*, 2019, **12**, 612–620.
11 S. Purohit, K. L. Yadav and S. Satapathi, *Langmuir*, 2021, **37**, 3467–3476.
12 S. Chen, K. Roh, J. Lee, W. K. Chong, Y. Lu, N. Mathews, T. C. Sum and A. Nurmikko, *ACS Nano*, 2016, **10**, 3959–3967.
13 M. M. Stylianakis, T. Maksudov, A. Panagiotopoulos, G. Kakavelakis and K. Petridis, *Materials*, 2019, **12**, 859.
14 X. Hu, X. Zhang, L. Liang, J. Bao, S. Li, W. Yang and Y. Xie, *Adv. Funct. Mater.*, 2014, **24**, 7373–7380.
15 H. Wang and D. H. Kim, *Chem. Soc. Rev.*, 2017, **46**, 5204–5236.
16 S. Yakunin, M. Sytnyk, D. Kriegner, S. Shrestha, M. Richter, G. J. Matt, H. Azimi, C. J. Brabec, J. Stangl, M. V. Kovalenko and W. Heiss, *Nat. Photonics*, 2015, **9**, 444–449.
17 H. Wei, Y. Fang, P. Mulligan, W. Chuirazzi, H.-H. Fang, C. Wang, B. R. Ecker, Y. Gao, M. A. Loi, L. Cao and J. Huang, *Nat. Photonics*, 2016, **10**, 333–339.
18 J.-P. Correa-Baena, M. Saliba, T. Buonassisi, M. Grätzel, A. Abate and W. Tress, *Science*, 2017, **358**, 739–744.
19 N.-G. Park, *Mater. Today*, 2015, **18**, 65–72.
20 S. Adjokatse, H.-H. Fang and M. A. Loi, *Mater. Today*, 2017, **20**, 413–424.
21 K. Lin, J. Xing, L. N. Quan, F. P. G. de Arquer, X. Gong, J. Lu, L. Xie, W. Zhao, D. Zhang, C. Yan, W. Li, X. Liu, Y. Lu, J. Kirman, E. H. Sargent, Q. Xiong and Z. Wei, *Nature*, 2018, **562**, 245–248.
22 S. A. Veldhuis, P. P. Boix, N. Yantara, M. Li, T. C. Sum, N. Mathews and S. G. Mhaisalkar, *Adv. Mater.*, 2016, **28**, 6804–6834.
23 J. Park, J. Kim, H. S. Yun, M. J. Paik, E. Noh, H. J. Mun, M. G. Kim, T. J. Shin and S. I. Seok, *Nature*, 2023, **616**, 724–730.
24 J. Peng, Y. Chen, K. Zheng, T. Pullerits and Z. Liang, *Chem. Soc. Rev.*, 2017, **46**, 5714–5729.
25 T. C. Sum and N. Mathews, *Energy Environ. Sci.*, 2014, **7**, 2518–2534.
26 H. Huang, B. Pradhan, J. Hofkens, M. B. J. Roeffaers and J. A. Steele, *ACS Energy Lett.*, 2020, **5**, 1107–1123.
27 K. Li, B. Peng and T. Peng, *ACS Catal.*, 2016, **6**, 7485–7527.
28 B.-M. Bresolin, Y. Park and D. Bahnemann, *Catalysts*, 2020, **10**, 709.
29 Z.-Y. Chen, N.-Y. Huang and Q. Xu, *Coord. Chem. Rev.*, 2023, **481**, 215031.

30 J. Yuan, H. Liu, S. Wang and X. Li, *Nanoscale*, 2021, **13**, 10281–10304.

31 H. Liu and S. Bansal, *Mater. Today Energy*, 2023, **32**, 101230.

32 Z. Zhang, S. Wang, X. Liu, Y. Chen, C. Su, Z. Tang, Y. Li and G. Xing, *Small Methods*, 2021, **5**, 2000937.

33 J. Wang, Y. Shi, Y. Wang and Z. Li, *ACS Energy Lett.*, 2022, **7**, 2043–2059.

34 E. M. Akinoglu, D. A. Hoogeveen, C. Cao, A. N. Simonov and J. J. Jasieniak, *ACS Nano*, 2021, **15**, 7860–7878.

35 H. Huang, D. Verhaeghe, B. Weng, B. Ghosh, H. Zhang, J. Hofkens, J. A. Steele and M. B. J. Roeffaers, *Angew. Chem., Int. Ed.*, 2022, **61**, 202203261.

36 X. Wang, J. He, X. Chen, B. Ma and M. Zhu, *Coord. Chem. Rev.*, 2023, **482**, 215076.

37 J. Wang, J. Liu, Z. Du and Z. Li, *J. Energy Chem.*, 2021, **54**, 770–785.

38 C. Han, X. Zhu, J. S. Martin, Y. Lin, S. Spears and Y. Yan, *ChemSusChem*, 2020, **13**, 4005–4025.

39 Q. A. Akkerman, G. Raino, M. V. Kovalenko and L. Manna, *Nat. Mater.*, 2018, **17**, 394–405.

40 S. Lee, G. Y. Jang, J. K. Kim and J. H. Park, *J. Energy Chem.*, 2021, **62**, 11–26.

41 M.-G. Ju, M. Chen, Y. Zhou, J. Dai, L. Ma, N. P. Padture and X. C. Zeng, *Joule*, 2018, **2**, 1231–1241.

42 Z.-L. Liu, R.-R. Liu, Y.-F. Mu, Y.-X. Feng, G.-X. Dong, M. Zhang and T.-B. Lu, *Sol. RRL*, 2021, **5**, 2000691.

43 J. Sheng, Y. He, J. Li, C. Yuan, H. Huang, S. Wang, Y. Sun, Z. Wang and F. Dong, *ACS Nano*, 2020, **14**, 13103–13114.

44 T. Chen, M. Zhou, W. Chen, Y. Zhang, S. Ou and Y. Liu, *Sustainable Energy Fuels*, 2021, **5**, 3598–3605.

45 L. Ding, F. Bai, B. Borjigin, Y. Li, H. Li and X. Wang, *Chem. Eng. J.*, 2022, **446**, 137102.

46 A. Mahmoud Idris, S. Zheng, L. Wu, S. Zhou, H. Lin, Z. Chen, L. Xu, J. Wang and Z. Li, *Chem. Eng. J.*, 2022, **446**, 137197.

47 J. Sheng, Y. He, M. Huang, C. Yuan, S. Wang and F. Dong, *ACS Catal.*, 2022, **12**, 2915–2926.

48 Y. Kim, E. Yassitepe, O. Voznyy, R. Comin, G. Walters, X. Gong, P. Kanjanaboos, A. F. Nogueira and E. H. Sargent, *ACS Appl. Mater. Interfaces*, 2015, **7**, 25007–25013.

49 M. Kovalenko, L. Protesescu and M. Bodnarchuk, *Science*, 2017, **358**, 745–750.

50 P. Chen, W. J. Ong, Z. Shi, X. Zhao and N. Li, *Adv. Funct. Mater.*, 2020, **30**, 1909667.

51 J. Liang, D. Chen, X. Yao, K. Zhang, F. Qu, L. Qin, Y. Huang and J. Li, *Small*, 2020, **16**, 1903398.

52 Y. F. Xu, M. Z. Yang, B. X. Chen, X. D. Wang, H. Y. Chen, D. B. Kuang and C. Y. Su, *J. Am. Chem. Soc.*, 2017, **139**, 5660–5663.

53 W. Yang, J. Noh, N. Jeon, Y. Kim, S. Ryu, J. Seo and S. Seok, *Science*, 2015, **348**, 9272.

54 X. Wang, J. He, J. Li, G. Lu, F. Dong, T. Majima and M. Zhu, *Appl. Catal., B*, 2020, **277**, 119230.

55 Y. F. Mu, W. Zhang, X. X. Guo, G. X. Dong, M. Zhang and T. B. Lu, *ChemSusChem*, 2019, **12**, 4769–4774.

56 Y. Yang, M. Yang, D. T. Moore, Y. Yan, E. M. Miller, K. Zhu and M. C. Beard, *Nat. Energy*, 2017, **2**, 16207.

57 Y. H. Kim, H. Cho and T. W. Lee, *Proc. Natl. Acad. Sci. U. S. A.*, 2016, **113**, 11694–11702.

58 Y. Yang, Y. Yan, M. Yang, S. Choi, K. Zhu, J. M. Luther and M. C. Beard, *Nat. Commun.*, 2015, **6**, 7961.

59 Q. Dong, Y. Fang, Y. Shao, P. Mulligan, J. Qiu, L. Cao and J. Huang, *Science*, 2015, **341**, 6225.

60 Q. Jiang, Y. Zhao, X. Zhang, X. Yang, Y. Chen, Z. Chu, Q. Ye, X. Li, Z. Yin and J. You, *Nat. Photonics*, 2019, **13**, 460–466.

61 K. Chen, S. Schunemann, S. Song and H. Tuysuz, *Chem. Soc. Rev.*, 2018, **47**, 7045–7077.

62 W.-J. Yin, T. Shi and Y. Yan, *J. Phys. Chem. C*, 2015, **119**, 5253–5264.

63 Q. V. Le, K. Hong, H. W. Jang and S. Y. Kim, *Adv. Electron. Mater.*, 2018, **4**, 1800335.

64 L. Protesescu, S. Yakunin, M. I. Bodnarchuk, F. Krieg, R. Caputo, C. H. Hendon, R. X. Yang, A. Walsh and M. V. Kovalenko, *Nano Lett.*, 2015, **15**, 3692–3696.

65 S.-H. Guo, J. Zhou, X. Zhao, C.-Y. Sun, S.-Q. You, X.-L. Wang and Z.-M. Su, *J. Catal.*, 2019, **369**, 201–208.

66 Z. Zhang, D. Li, H. Hu, Y. Chu and J. Xu, *Inorg. Chem.*, 2023, **62**, 9240–9248.

67 G. Xing, N. Mathews, S. Sun, S. S. Lim, Y. M. Lam, M. Gratzel, S. Mhaisalkar and T. C. Sum, *Science*, 2013, **342**, 344–347.

68 J. Tauc, *Rev. Mod. Phys.*, 1957, **29**, 308–324.

69 Y. H. Kim, J. S. Kim and T. W. Lee, *Adv. Mater.*, 2019, **31**, 1804595.

70 Z. H. Yan, M. H. Du, J. Liu, S. Jin, C. Wang, G. L. Zhuang, X. J. Kong, L. S. Long and L. S. Zheng, *Nat. Commun.*, 2018, **9**, 3353.

71 H. L. Wu, X. B. Li, C. H. Tung and L. Z. Wu, *Adv. Mater.*, 2019, **31**, 1900709.

72 K. Ray, F. F. Pfaff, B. Wang and W. Nam, *J. Am. Chem. Soc.*, 2014, **136**, 13942–13958.

73 S. G. Shetty, I. M. Ciobica, E. J. Hensen and R. A. van Santen, *Chem. Commun.*, 2011, **47**, 9822–9824.

74 S. Park, W. J. Chang, C. W. Lee, S. Park, H.-Y. Ahn and K. T. Nam, *Nat. Energy*, 2016, **2**, 16185.

75 H. Luo, S. Guo, Y. Zhang, K. Bu, H. Lin, Y. Wang, Y. Yin, D. Zhang, S. Jin, W. Zhang, W. Yang, B. Ma and X. Lu, *Adv. Sci.*, 2021, **8**, 2100786.

76 Y. Lin, Y. Shao, J. Dai, T. Li, Y. Liu, X. Dai, X. Xiao, Y. Deng, A. Gruverman, X. C. Zeng and J. Huang, *Nat. Commun.*, 2021, **12**, 7.

77 F. Hao, C. C. Stoumpos, D. H. Cao, R. P. H. Chang and M. G. Kanatzidis, *Nat. Photonics*, 2014, **8**, 489–494.

78 M. Chen, M. G. Ju, H. F. Garces, A. D. Carl, L. K. Ono, Z. Hawash, Y. Zhang, T. Shen, Y. Qi, R. L. Grimm, D. Pacifici, X. C. Zeng, Y. Zhou and N. P. Padture, *Nat. Commun.*, 2019, **10**, 16.

79 D. Wu, Y. Tao, Y. Huang, B. Huo, X. Zhao, J. Yang, X. Jiang, Q. Huang, F. Dong and X. Tang, *J. Catal.*, 2021, **397**, 27–35.

80 Z. Chen, X. Li, Y. Wu, J. Zheng, P. Peng, X. Zhang, A. Duan, D. Wang and Q. Yang, *Sep. Purif. Technol.*, 2022, **295**, 121250.

81 T. Wang, D. Yue, X. Li and Y. Zhao, *Appl. Catal., B*, 2020, **268**, 118399.

82 Y. Zhang, Z. Sun, Z. Wang, Y. Zang and X. Tao, *Int. J. Hydrogen Energy*, 2022, **47**, 8829–8840.

83 H. Lv, H. Yin, N. Jiao, C. Yuan, S. Weng, K. Zhou, Y. Dang, X. Wang, Z. Lu and Y. Zhang, *Small Methods*, 2023, **7**, 2201365.

84 L. Zhou, Y. F. Xu, B. X. Chen, D. B. Kuang and C. Y. Su, *Small*, 2018, **14**, 1703762.

85 Z. Liu, H. Yang, J. Wang, Y. Yuan, K. Hills-Kimball, T. Cai, P. Wang, A. Tang and O. Chen, *Nano Lett.*, 2021, **21**, 1620–1627.

86 Y.-X. Feng, G.-X. Dong, K. Su, Z.-L. Liu, W. Zhang, M. Zhang and T.-B. Lu, *J. Energy Chem.*, 2022, **69**, 348–355.

87 S. Sun, D. Yuan, Y. Xu, A. Wang and Z. Deng, *ACS Nano*, 2016, **10**, 3648–3657.

88 A. P. Alivisatos, W. Gu and C. Larabell, *Annu. Rev. Biomed. Eng.*, 2005, **7**, 55–76.

89 C. Huo, B. Cai, Z. Yuan, B. Ma and H. Zeng, *Small Methods*, 2017, **1**, 1600018.

90 J. Xing, Y. Zhao, M. Askerka, L. N. Quan, X. Gong, W. Zhao, J. Zhao, H. Tan, G. Long, L. Gao, Z. Yang, O. Voznyy, J. Tang, Z. H. Lu, Q. Xiong and E. H. Sargent, *Nat. Commun.*, 2018, **9**, 3541.

91 M. Ahmadi, T. Wu and B. Hu, *Adv. Mater.*, 2017, **29**, 1605242.

92 L.-Y. Wu, M.-R. Zhang, Y.-X. Feng, W. Zhang, M. Zhang and T.-B. Lu, *Sol. RRL*, 2021, **5**, 2100263.

93 J. Pi, X. Jia, Z. Long, S. Yang, H. Wu, D. Zhou, Q. Wang, H. Zheng, Y. Yang, J. Zhang and J. Qiu, *Adv. Energy Mater.*, 2022, **12**, 2202074.

94 K. Li, X. An, K. H. Park, M. Khraisheh and J. Tang, *Catal. Today*, 2014, **224**, 3–12.

95 Y. Sun, X. Meng, Y. Dall'Agnese, C. Dall'Agnese, S. Duan, Y. Gao, G. Chen and X. F. Wang, *Nano-Micro Lett.*, 2019, **11**, 79.

96 Y. Xu, M.-Z. Yang, H.-Y. Chen, J.-F. Liao, X.-D. Wang and D.-B. Kuang, *ACS Appl. Energy Mater.*, 2018, **1**, 5083–5089.

97 Y.-X. Chen, Y.-F. Xu, X.-D. Wang, H.-Y. Chen and D.-B. Kuang, *Sustainable Energy Fuels*, 2020, **4**, 2249–2255.

98 J.-F. Liao, Y.-T. Cai, J.-Y. Li, Y. Jiang, X.-D. Wang, H.-Y. Chen and D.-B. Kuang, *J. Energy Chem.*, 2021, **53**, 309–315.

99 R. Tang, H. Sun, Z. Zhang, L. Liu, F. Meng, X. Zhang, W. Yang, Z. Li, Z. Zhao, R. Zheng and J. Huang, *Chem. Eng. J.*, 2022, **429**, 132137.

100 Z. Zhang, D. Li, Y. Chu, L. Chang and J. Xu, *J. Phys. Chem. Lett.*, 2023, **14**, 5249–5259.

101 Z.-C. Kong, H.-H. Zhang, J.-F. Liao, Y.-J. Dong, Y. Jiang, H.-Y. Chen and D.-B. Kuang, *Sol. RRL*, 2019, **4**, 1900365.

102 Z. Chen, Y. Hu, J. Wang, Q. Shen, Y. Zhang, C. Ding, Y. Bai, G. Jiang, Z. Li and N. Gaponik, *Chem. Mater.*, 2020, **32**, 1517–1525.

103 J. Wang, T. Xia, L. Wang, X. Zheng, Z. Qi, C. Gao, J. Zhu, Z. Li, H. Xu and Y. Xiong, *Angew. Chem., Int. Ed.*, 2018, **57**, 16447–16451.

104 C. H. Lu, G. V. Biesold-McGee, Y. Liu, Z. Kang and Z. Lin, *Chem. Soc. Rev.*, 2020, **49**, 4953–5007.

105 C. Tang, C. Chen, W. Xu and L. Xu, *J. Mater. Chem. A*, 2019, **7**, 6911–6919.

106 Y. W. Liu, S. H. Guo, S. Q. You, C. Y. Sun, X. L. Wang, L. Zhao and Z. M. Su, *Nanotechnology*, 2020, **31**, 215605.

107 S. Shyamal, S. K. Dutta, T. Das, S. Sen, S. Chakraborty and N. Pradhan, *J. Phys. Chem. Lett.*, 2020, **11**, 3608–3614.

108 Z.-Y. Chen, Q.-L. Hong, H.-X. Zhang and J. Zhang, *ACS Appl. Mater. Interfaces*, 2021, **5**, 1175–1182.

109 Z. Cui, P. Wang, Y. Wu, X. Liu, G. Chen, P. Gao, Q. Zhang, Z. Wang, Z. Zheng, H. Cheng, Y. Liu, Y. Dai and B. Huang, *Appl. Catal., B*, 2022, **310**, 121375.

110 Z. Zhang, D. Li, Z. Dong, Y. Jiang, X. Li, Y. Chu and J. Xu, *Sol. RRL*, 2023, **7**, 2300038.

111 M. Ou, W. Tu, S. Yin, W. Xing, S. Wu, H. Wang, S. Wan, Q. Zhong and R. Xu, *Angew. Chem., Int. Ed.*, 2018, **57**, 13570–13574.

112 Y. Xu, W. Zhang, K. Su, Y. X. Feng, Y. F. Mu, M. Zhang and T. B. Lu, *Chem. – Eur. J.*, 2021, **27**, 2305–2309.

113 X. D. Wang, Y. H. Huang, J. F. Liao, Y. Jiang, L. Zhou, X. Y. Zhang, H. Y. Chen and D. B. Kuang, *J. Am. Chem. Soc.*, 2019, **141**, 13434–13441.

114 N. Li, X. Chen, J. Wang, X. Liang, L. Ma, X. Jing, D. L. Chen and Z. Li, *ACS Nano*, 2022, **16**, 3332–3340.

115 S. Wan, M. Ou, Q. Zhong and X. Wang, *Chem. Eng. J.*, 2019, **358**, 1287–1295.

116 A. Bard, *J. Photochem.*, 1979, **10**, 59–75.

117 J. Yu, S. Wang, J. Low and W. Xiao, *Phys. Chem. Chem. Phys.*, 2013, **15**, 16883–16890.

118 F. Xu, K. Meng, B. Cheng, S. Wang, J. Xu and J. Yu, *Nat. Commun.*, 2020, **11**, 4613.

119 T. Chen, L. Liu, C. Hu and H. Huang, *Chin. J. Catal.*, 2021, **42**, 1413–1438.

120 Z. Jiang, X. Liang, H. Zheng, Y. Liu, Z. Wang, P. Wang, X. Zhang, X. Qin, Y. Dai, M.-H. Whangbo and B. Huang, *Appl. Catal., B*, 2017, **219**, 209–215.

121 J. Wang, J. Wang, N. Li, X. Du, J. Ma, C. He and Z. Li, *ACS Appl. Mater. Interfaces*, 2020, **12**, 31477–31485.

122 Y. Feng, D. Chen, Y. Zhong, Z. He, S. Ma, H. Ding, W. Ao, X. Wu and M. Niu, *ACS Appl. Mater. Interfaces*, 2023, **15**, 9221–9230.

123 L. Tan, S. M. Xu, Z. Wang, Y. Xu, X. Wang, X. Hao, S. Bai, C. Ning, Y. Wang, W. Zhang, Y. K. Jo, S. J. Hwang, X. Cao, X. Zheng, H. Yan, Y. Zhao, H. Duan and Y. F. Song, *Angew. Chem., Int. Ed.*, 2019, **58**, 11860–11867.

124 K. Wang, L. Zhang, Y. Su, D. Shao, S. Zeng and W. Wang, *J. Mater. Chem. A*, 2018, **6**, 8366–8373.

125 S. Zhao, Q. Liang, Z. Li, H. Shi, Z. Wu, H. Huang and Z. Kang, *Nano Res.*, 2022, **15**, 5953–5961.

126 M. Liu, K. Jiang, X. Ding, S. Wang, C. Zhang, J. Liu, Z. Zhan, G. Cheng, B. Li, H. Chen, S. Jin and B. Tan, *Adv. Mater.*, 2019, **31**, 1807865.

127 Z. Zhang, Y. Jiang, Z. Dong, Y. Chu and J. Xu, *Inorg. Chem.*, 2022, **61**, 16028–16037.

128 H. Rao, L. C. Schmidt, J. Bonin and M. Robert, *Nature*, 2017, **548**, 74–77.

129 K. Thampi, J. Kiwi and M. Grtzel, *Nature*, 1987, **327**, 11.

130 Q. M. Sun, J. J. Xu, F. F. Tao, W. Ye, C. Zhou, J. H. He and J. M. Lu, *Angew. Chem., Int. Ed.*, 2022, **61**, 202200872.

131 S. Bera, S. Shyamal and N. Pradhan, *J. Am. Chem. Soc.*, 2021, **143**, 14895–14906.

132 A. E. Farrell, R. J. Plevin, B. T. Turner, A. D. Jones, M. O'Hare and D. M. Kammen, *Science*, 2006, **311**, 506–508.

133 A. Banerjee, G. R. Dick, T. Yoshino and M. W. Kanan, *Nature*, 2016, **531**, 215–219.

134 J. Li, A. Xu, F. Li, Z. Wang, C. Zou, C. M. Gabardo, Y. Wang, A. Ozden, Y. Xu, D. H. Nam, Y. Lum, J. Wicks, B. Chen, Z. Wang, J. Chen, Y. Wen, T. Zhuang, M. Luo, X. Du, T. K. Sham, B. Zhang, E. H. Sargent and D. Sinton, *Nat. Commun.*, 2020, **11**, 3685.

135 L. Kong, Z. Chen, Q. Cai, L. Yin and J. Zhao, *Chin. Chem. Lett.*, 2022, **33**, 2183–2187.

136 A. R. Woldu, Z. Huang, P. Zhao, L. Hu and D. Astruc, *Coord. Chem. Rev.*, 2022, **454**, 214340.

137 D. Voiry, H. S. Shin, K. P. Loh and M. Chhowalla, *Nat. Rev. Chem.*, 2018, **2**, 0105.

138 T. T. Zhuang, Z. Q. Liang, A. Seifitokaldani, Y. Li, P. De Luna, T. Burdyny, F. Che, F. Meng, Y. Min, R. Quintero-Bermudez, C. T. Dinh, Y. Pang, M. Zhong, B. Zhang, J. Li, P. N. Chen, X. L. Zheng, H. Liang, W. N. Ge, B.-J. Ye, D. Sinton, S. H. Yu and E. H. Sargent, *Nat. Catal.*, 2018, **1**, 421–428.

139 Y. Zheng, A. Vasileff, X. Zhou, Y. Jiao, M. Jaroniec and S. Z. Qiao, *J. Am. Chem. Soc.*, 2019, **141**, 7646–7659.

140 W. Ma, X. He, W. Wang, S. Xie, Q. Zhang and Y. Wang, *Chem. Soc. Rev.*, 2021, **50**, 12897–12914.

141 B. N. Choi, J. Y. Seo, Z. An, P. J. Yoo and C.-H. Chung, *Chem. Eng. J.*, 2022, **430**, 132807.

142 S. Peng, Z. Yang, M. Sun, L. Yu and Y. Li, *Adv. Mater.*, 2023, **35**, e2304711.

143 Y. Han, S. Yue and B. B. Cui, *Adv. Sci.*, 2021, **8**, e2004805.

144 H. Zhao, K. Kordas and S. Ojala, *J. Mater. Chem. A*, 2023, **11**, 22656–22687.

145 Z. J. Li, E. Hofman, J. Li, A. H. Davis, C. H. Tung, L. Z. Wu and W. Zheng, *Adv. Funct. Mater.*, 2017, **28**, 1704288.

146 S. S. Bhosale, A. K. Kharade, E. Jokar, A. Fathi, S. M. Chang and E. W. Diau, *J. Am. Chem. Soc.*, 2019, **141**, 20434–20442.

147 J. Albero, Y. Peng and H. García, *ACS Catal.*, 2020, **10**, 5734–5749.

148 X. Zhang, F. Han, B. Shi, S. Farsinezhad, G. P. Dechaine and K. Shankar, *Angew. Chem., Int. Ed.*, 2012, **51**, 12732–12735.

149 H. Park, H. H. Ou, A. J. Colussi and M. R. Hoffmann, *J. Phys. Chem. A*, 2015, **119**, 4658–4666.

150 I. Shown, H. C. Hsu, Y. C. Chang, C. H. Lin, P. K. Roy, A. Ganguly, C. H. Wang, J. K. Chang, C. I. Wu, L. C. Chen and K. H. Chen, *Nano Lett.*, 2014, **14**, 6097–6103.

151 Y. Hori, A. Murata, R. Takahashi and S. Suzuki, *J. Am. Chem. Soc.*, 1987, **109**, 5022–5023.

152 R. Kortlever, J. Shen, K. J. Schouten, F. Calle-Vallejo and M. T. Koper, *J. Phys. Chem. Lett.*, 2015, **6**, 4073–4082.

153 X. Chang, T. Wang, P. Yang, G. Zhang and J. Gong, *Adv. Mater.*, 2019, **31**, e1804710.

154 W. Liu, W. Hu, L. Yang and J. Liu, *Nano Energy*, 2020, **73**, 104750.

155 N. S. Weliwatte and S. D. Minteer, *Joule*, 2021, **5**, 2564–2592.

156 H. Salehizadeh, N. Yan and R. Farnood, *Chem. Eng. J.*, 2020, **390**, 124584.

157 S. Bajracharya, S. Srikanth, G. Mohanakrishna, R. Zacharia, D. P. Strik and D. Pant, *J. Power Sources*, 2017, **356**, 256–273.

158 R. Das, S. Chakraborty and S. C. Peter, *ACS Energy Lett.*, 2021, **6**, 3270–3274.

159 J. S. Martin, N. Dang, E. Raulerson, M. C. Beard, J. Hartenberger and Y. Yan, *Angew. Chem., Int. Ed.*, 2022, **61**, e20220557.

160 Y. Zhang, L. Shi, H. Yuan, X. Sun, X. Li, L. Duan, Q. Li, Z. Huang, X. Ban and D. Zhang, *Chem. Eng. J.*, 2022, **430**, 132820.

161 S. Xu, L. Yang, Y. Wei, Y. Jia, M. Hu, L. Bai, J. Zhang, X. Li, S. Wei and J. Lu, *Dalton Trans.*, 2022, **51**, 8036–8045.

162 Y. H. Chen, J. K. Ye, Y. J. Chang, T. W. Liu, Y. H. Chuang, W. R. Liu, S. H. Liu and Y. C. Pu, *Appl. Catal., B*, 2021, **284**, 119751.

163 J. C. Wang, N. Li, A. M. Idris, J. Wang, X. Du, Z. Pan and Z. Li, *Sol. RRL*, 2021, **5**, 2100154.

164 Y. X. Chen, Y. F. Xu, X. D. Wang, H. Y. Chen and D. B. Kuang, *Sustainable Energy Fuels*, 2020, **4**, 2249–2255.

165 X. Li, J. Liu, G. Jiang, X. Lin, J. Wang and Z. Li, *J. Colloid Interface Sci.*, 2023, **643**, 174–182.

166 J. Hou, S. Cao, Y. Wu, Z. Gao, F. Liang, Y. Sun, Z. Lin and L. Sun, *Chem. – Eur. J.*, 2017, **23**, 9481–9485.

167 Q. Wang, J. Wang, J. C. Wang, X. Hu, Y. Bai, X. Zhong and Z. Li, *ChemSusChem*, 2021, **14**, 1131–1139.

168 Y. F. Xu, M. Z. Yang, H. Y. Chen, J. F. Liao, X. D. Wang and D. B. Kuang, *ACS Appl. Mater. Interfaces*, 2018, **1**, 5083–5089.

169 Y. J. Dong, Y. Jiang, J. F. Liao, H.-Y. Chen, D. B. Kuang and C.-Y. Su, *Sci. China Mater.*, 2022, **65**, 1550–1559.

170 X. Jiang, Y. Ding, S. Zheng, Y. Ye, Z. Li, L. Xu, J. Wang, Z. Li, X. J. Loh, E. Ye and L. Sun, *ChemSusChem*, 2022, **15**, 202102295.

171 X. Wang, J. He, L. Mao, X. Cai, C. Sun and M. Zhu, *Chem. Eng. J.*, 2021, **416**, 128077.

172 L. Li, Z. Zhang, C. Ding and J. Xu, *Chem. Eng. J.*, 2021, **419**, 129543.

173 K. Su, G. X. Dong, W. Zhang, Z. L. Liu, M. Zhang and T. B. Lu, *ACS Appl. Mater. Interfaces*, 2020, **12**, 50464–50471.

174 Z. Zhang, M. Shu, Y. Jiang and J. Xu, *Chem. Eng. J.*, 2021, **414**, 128889.

175 Z. Dong, Y. Shi, Y. Jiang, C. Yao and Z. Zhang, *J. CO_2* Util., 2023, **72**, 102480.

176 Z. Zhang, Z. Dong, Y. Jiang, Y. Chu and J. Xu, *Chem. Eng. J.*, 2022, **435**, 135014.
177 Z. Zhang, L. Li, Y. Jiang and J. Xu, *Inorg. Chem.*, 2022, **61**, 3351–3360.
178 R. Cheng, E. Debroye, J. Hofkens and M. B. J. Roeffaers, *Catalysts*, 2020, **10**, 1352.
179 L. Ding, B. Borjigin, Y. Li, X. Yang, X. Wang and H. Li, *ACS Appl. Mater. Interfaces*, 2021, **13**, 51161–51173.
180 Y. Xi, X. Zhang, Y. Shen, W. Dong, Z. Fan, K. Wang, S. Zhong and S. Bai, *Appl. Catal., B*, 2021, **297**, 120411.
181 J. Hu, M. Yang, X. Ke, S. Yang, K. Wang, H. Huang, W. Wang, D. Luo, Z. Zheng, L. Huang, P. Xiao, C. Tu, Y. Min, N. Huo and M. Zhang, *J. Power Sources*, 2021, **481**, 228838.
182 J. Wang, L. Xiong, Y. Bai, Z. Chen, Q. Zheng, Y. Shi, C. Zhang, G. Jiang and Z. Li, *Sol. RRL*, 2022, **6**, 2200294.
183 Z. Dong, Z. Zhang, Y. Jiang, Y. Chu and J. Xu, *Chem. Eng. J.*, 2022, **433**, 133762.
184 Y. Jiang, Y. Wang, Z. Zhang, Z. Dong and J. Xu, *Inorg. Chem.*, 2022, **61**, 10557–10566.
185 D. Li, J. Zhou, Z. Zhang, Y. Jiang, Z. Dong, J. Xu and C. Yao, *ACS Appl. Mater. Interfaces*, 2022, **5**, 6238–6247.
186 Y. Jiang, C. Mei, Z. Zhang and Z. Dong, *Dalton Trans.*, 2021, **50**, 16711–16719.
187 M. Xiao, M. Hao, M. Lyu, E. G. Moore, C. Zhang, B. Luo, J. Hou, J. Lipton-Duffin and L. Wang, *Adv. Funct. Mater.*, 2019, **29**, 1905683.
188 J. Zhu, Y. Zhu, J. Huang, L. Hou, J. Shen and C. Li, *Nanoscale*, 2020, **12**, 11842–11846.
189 G. Zhang, X. Ke, X. Liu, H. Liao, W. Wang, H. Yu, K. Wang, S. Yang, C. Tu, H. Gu, D. Luo, L. Huang and M. Zhang, *ACS Appl. Mater. Interfaces*, 2022, **14**, 44909–44921.
190 Y. Gong, J. Shen, Y. Zhu, W. Yan, J. Zhu, L. Hou, D. Xie and C. Li, *Appl. Surf. Sci.*, 2021, **545**, 149012.
191 M. Shu, Z. Zhang, Z. Dong and J. Xu, *Carbon*, 2021, **182**, 454–462.
192 N. Zhang, J. J. Li, Y. Li, H. Wang, J. Y. Zhang, Y. Liu, Y. Z. Fang, Z. Liu and M. Zhou, *J. Colloid Interface Sci.*, 2022, **608**, 3192–3203.
193 J. Bian, C. Huang and R. Q. Zhang, *ChemSusChem*, 2016, **9**, 2723–2735.
194 S.-X. Yuan, K. Su, Y.-X. Feng, M. Zhang and T.-B. Lu, *Chin. Chem. Lett.*, 2023, **34**, 107682.
195 Y. F. Mu, W. Zhang, G. X. Dong, K. Su, M. Zhang and T. B. Lu, *Small*, 2020, **16**, 2002140.
196 A. Pan, X. Ma, S. Huang, Y. Wu, M. Jia, Y. Shi, Y. Liu, P. Wangyang, L. He and Y. Liu, *J. Phys. Chem. Lett.*, 2019, **10**, 6590–6597.
197 D. Wu, C. Tian, J. Zhou, Y. Huang, J. Lai, B. Gao, P. He, Q. Huang and X. Tang, *Carbon Neutralization*, 2022, **1**, 298–305.
198 C. Lu, D. S. Itanze, A. G. Aragon, X. Ma, H. Li, K. B. Ucer, C. Hewitt, D. L. Carroll, R. T. Williams, Y. Qiu and S. M. Geyer, *Nanoscale*, 2020, **12**, 2987–2991.
199 S. S. Bhosale, A. K. Kharade, E. Jokar, A. Fathi, S. M. Chang and E. W. Diau, *J. Am. Chem. Soc.*, 2019, **141**, 20434–20442.
200 Y. Jiang, R. Zhou, Z. Z. Zhang, Z. L. Dong and J. Y. Xu, *J. Mater. Chem. C*, 2023, **11**, 2540.
201 L. Wu, S. Zheng, H. Lin, S. Zhou, A. Mahmoud Idris, J. Wang, S. Li and Z. Li, *J. Colloid Interface Sci.*, 2023, **629**, 233–242.
202 Y. Wang, Q. Zhou, Y. Zhu and D. Xu, *Appl. Catal., B*, 2021, **294**, 120236.
203 S. Cheng, X. Chen, M. Wang, G. Li, X. Qi, Y. Tian, M. Jia, Y. Han, D. Wu, X. Li and Z. Shi, *Appl. Surf. Sci.*, 2023, **621**, 156877.
204 N. Li, X.-P. Zhai, B. Ma, H.-J. Zhang, M.-J. Xiao, Q. Wang and H.-L. Zhang, *J. Mater. Chem. A*, 2023, **11**, 4020–4029.
205 D. Wu, B. Huo, Y. Huang, X. Zhao, J. Yang, K. Hu, X. Mao, P. He, Q. Huang and X. Tang, *Small*, 2022, **18**, 2106001.
206 C. Tian, Q. Huang, D. Wu, J. Lai, F. Qi, N. Zhang, W. Zhang and X. Tang, *Mater. Today Energy*, 2022, **28**, 101067.
207 Q. Huang, C. Tian, J. Lai, F. Qi, N. Zhang, J. Liu, Z. Liang, D. Wu and X. Tang, *Inorg. Chem.*, 2022, **61**, 14447–14454.
208 J. Liu, Z. Wu, F. Zhang, M. Zhao, C. Li, J. Li, B. Wen and F. Wang, *Nanoscale*, 2023, **15**, 7023–7031.
209 S. Kumar, I. Hassan, M. Regue, S. Gonzalez-Carrero, E. Rattner, M. A. Isaacs and S. Eslava, *J. Mater. Chem. A*, 2021, **9**, 12179.
210 S. Bera, A. Patra, S. Shyamal, D. Nasipuri and N. Pradhan, *ACS Energy Lett.*, 2022, **7**, 3015–3023.
211 Y. F. Xu, X. D. Wang, J. F. Liao, B. X. Chen, H. Y. Chen and D. B. Kuang, *Adv. Mater. Interfaces*, 2018, **5**, 1801015.
212 Z. C. Kong, J. F. Liao, Y. J. Dong, Y. F. Xu, H. Y. Chen, D. B. Kuang and C. Y. Su, *ACS Energy Lett.*, 2018, **3**, 2656–2662.
213 Y. F. Xu, M. Z. Yang, B. X. Chen, X. D. Wang, H. Y. Chen, D. B. Kuang and C. Y. Su, *J. Am. Chem. Soc.*, 2017, **139**, 5660–5663.
214 Y. Jiang, J. F. Liao, Y. F. Xu, H. Y. Chen, X. D. Wang and D. B. Kuang, *J. Mater. Chem. A*, 2019, **7**, 13762.
215 Y. Jiang, J. F. Liao, H. Y. Chen, H. H. Zhang, J. Y. Li, X. D. Wang and D. B. Kuang, *Chem*, 2020, **6**, 766–780.
216 S. Kumar, M. Regue, M. A. Isaacs, E. Freeman and S. Eslava, *ACS Appl. Energy Mater.*, 2020, **3**, 4509–4522.